

Generative Classifiers as a Basis for Trustworthy Computer Vision

Radek Mackowiak*

Visual Learning Lab, Heidelberg University

Ullrich Köthe

Visual Learning Lab, Heidelberg University

Lynton Ardizzone*

Visual Learning Lab, Heidelberg University

Carsten Rother

Visual Learning Lab, Heidelberg University

* equal contribution

Abstract

With the maturing of deep learning systems, trustworthiness is becoming increasingly important for model assessment. We understand trustworthiness as the combination of explainability and robustness. Generative classifiers (GCs) are a promising class of models that are said to naturally accomplish these qualities. However, this has mostly been demonstrated on simple datasets such as MNIST, SVHN and CIFAR in the past. In this work, we firstly develop an architecture and training scheme that allows for GCs to be trained on the ImageNet classification task, a more relevant level of complexity for practical computer vision. The resulting models use an invertible neural network architecture and achieve a competitive ImageNet top-1 accuracy of up to 76.2%. Secondly, we show the large potential of GCs for trustworthiness. Explainability and some aspects of robustness are vastly improved compared to standard feed-forward models, even when the GCs are just applied naively. While not all trustworthiness problems are solved completely, we argue from our observations that GCs are an extremely promising basis for further algorithms and modifications, as have been developed in the past for feed-forward models to increase their trustworthiness. We release our trained model for download in the hope that it serves as a starting point for various other generative classification tasks in much the same way as pretrained ResNet models do for discriminative classification.

Code: github.com/VLL-HD/trustworthy_GCs

1. Introduction

Generative classifiers (GCs) and discriminative classifiers (DCs) represent two contrasting ways of solving classification tasks. In short, while standard DCs model the class probability given an input directly, $p(\text{class} | \text{image})$ (e.g. softmax classification), generative classifiers (GCs) take the opposite approach: They model the likelihood of the input

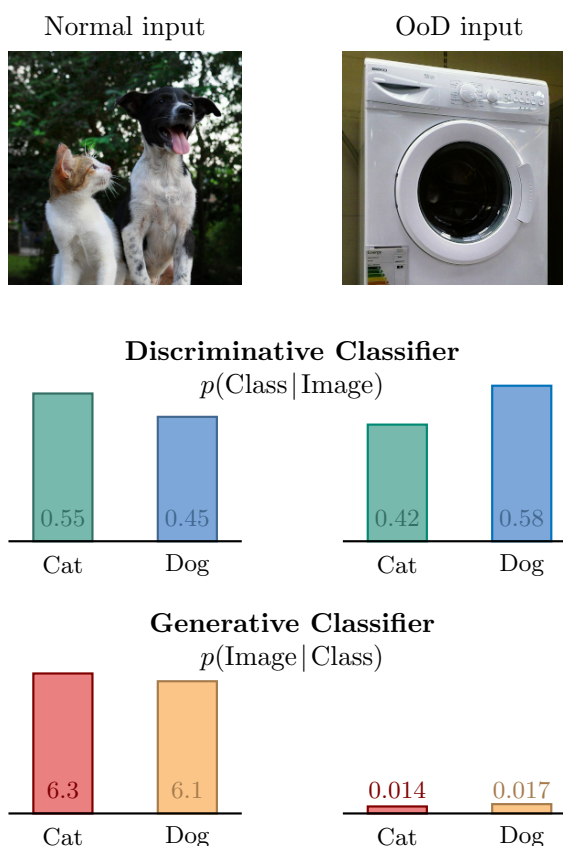


Figure 1: Example for one of the advantages of generative classifiers: The class posterior of a DC always sums to 1. The image likelihoods of the GC do not have this restriction. From this, the GC can show whether a prediction is uncertain because the input agrees with both classes, or with neither. For the DC, there is no difference between these two cases. The small numbers in the bars are exemplary output probabilities.

image, conditioned on each class, $p(\text{image} \mid \text{class})$. The actual classification is then performed by finding the class under which the image has the highest likelihood. To clarify the terminology: the main use of a GC is not to generate some new images (although this is certainly possible, by sampling from the learned distribution); DCs and GCs both get an image as input, and output probabilities. The difference is in whether these are posterior class probabilities, or probability densities of images conditioned on each class.

Because of the increased complexity of the task, the application of GCs has been limited to very simple datasets such as MNIST, SVHN and CIFAR-10/100 in the past. For any practical or real-world computer vision applications, DCs are used exclusively, due to their excellent discriminative performance. In principle however, GCs are said to have various advantages over DCs, which align with the term *trustworthiness*. In general agreement with [26], we understand trustworthiness mainly as the combination of explainability and robustness.

Explainability Deep neural network based DCs are notorious for being ‘black boxes’, prompting many developments in the field of explainable AI. In the taxonomy laid out in [19], most commonly used algorithms fall into categories I or II, meaning they attempt to visualize how the network processes information, or its internal representations, in a post-hoc manner. In this case, the explanation obtained can vary depending on the method used or the hyperparameters, and there is no guarantee that the results truly reflect what the DC is doing internally. In contrast, GCs bring to mind Feynman’s mantra “What I cannot create, I do not understand”. As GCs are able to model the input data itself, not just the class posteriors, they have fundamentally more informative outputs. For instance, GCs allow us to tell if a decision between two classes is uncertain because the input agrees well with *both* classes, or with *neither* (see Fig. 1). In addition, most types of GCs have interpretable latent spaces with meaningful features. Through this, the actual decision process can be directly visualized, without relying on post-hoc techniques. The latent space brings other advantages too, such as analyzing inter- and intra-class relationships (Fig. 19). In these ways, GCs could be argued to belong to category III of the explainability taxonomy [19], i.e. methods that intrinsically work in an explainable way, without additional algorithms.

Robustness A second large concern about practical use of deep learning systems is their robustness, which can have different meanings, depending on the context and area of research. In particular, GCs have been assumed to be superior to DCs in terms of generalization under dataset shifts [41] and accurately calibrated uncertainties [3]. The latter is especially critical, DCs often make highly confident predictions, even when the input is completely unrelated to the training data [23, 47, 12]. A secondary aspect of robustness

is the explicit detection of abnormal or out-of-distribution (OoD) inputs. Returning to the example from Fig. 1, we can imagine it is easy for GCs to explicitly detect the second OoD case by using a threshold on the predicted probability. The user or system can then be notified that the input is OoD, and the decision should not be trusted. Lastly, in the context of adversarial attacks, robustness is commonly understood as the difficulty of finding a successful attack. For a more ‘robust’ model in this sense, the adversarial perturbations will be larger, and in the best case the attack will fail entirely. GCs were found to be more robust towards adversarial attacks than DCs [34], and attacks can also be explicitly detected.

While all these advantages are well-known and have been observed for simple datasets, it has so far remained unclear whether they also apply for more complex tasks, and whether GCs can be used in this case. For example, the authors of [16] find while GCs correctly assign lower likelihoods on adversarially perturbed images in the case of MNIST, they do not for the more complex CIFAR-10 dataset. The authors of [35] observe that OoD detection using generative likelihood models fails in various ways when applied to natural images. In [17], the authors cast doubt on whether GCs can be used for high-dimensional input data at all. To further investigate potential issues arising from dataset complexity, and properly demonstrate the potential of GCs for computer vision, we train a GC on the ImageNet dataset. We choose this dataset specifically for three reasons: Firstly, it remains a moderately challenging task, even for modern deep neural networks, and is therefore a useful benchmark for our purposes. Secondly, the data is easily understandable by humans, making it suitable for demonstrating explainability techniques. Lastly, due to the diverse nature of the dataset, networks pre-trained on ImageNet are usually used as the starting point for solving other practical tasks; pre-trained ResNets or VGG networks are ubiquitous in current deep learning research. The first step in adopting GCs for practical applications should therefore be the same: Providing pre-trained models suitable for a wide variety of complex tasks to enable building more explainable, robust and therefore more trustworthy computer vision systems.

To summarize, this work shows that GCs can perform at a level relevant to practical applications. We find that naively applied GCs do not solve all aspects of trustworthiness ipso facto, but that they offer significant improvements and a more advantageous starting point compared to feed forward models in the goal of fully trustworthy computer vision. Our contributions are the following:

- We show the technical changes necessary to reach competitive classification performance using a GC for ImageNet. Our model achieves up to 76.2% top-1 accuracy. A similar standard ResNet model achieves 77.4% [22].

- We demonstrate various techniques for explainability that are unique to GCs. Without any additional algorithms, it is possible to natively visualize decision processes, class relationships, and properties of OoD data.
- We examine different aspects of the robustness of the GC model. While measurably more robust to adversarial attacks, we cannot extend the claims that GCs are virtually immune to them [18, 43]; nor do we find significantly better generalization under various image corruptions. On the other hand, both cases can be explicitly detected fairly reliably by utilizing OoD tests only applicable to generative models.

2. Related Work

Years before the deep learning revolution, works such as [38, 52, 41] already compared the properties of GCs vs DCs, theoretically and experimentally. While the question of task performance varies across works, most agree that GCs are more robust and more explainable. Works like [6, 5, 55] presented models that combine the aspects of GCs and DCs, to reach a more favourable trade-off compared to each extreme. However, all these works consider comparatively simple problems, suited to the models of the time. Later, with the unmatched task performance that deep-learning based DCs delivered in the 2010s, GCs became rarely used.

As one example of more recent work, [17] investigates normalizing-flow based GCs trained on natural images. The authors find that naively trained conditional likelihood models achieve very poor classification performance, and argue that this is due to some model properties that are not properly penalized by maximum likelihood training. Later, [3] propose that this problem can be avoided by training with the Information Bottleneck loss function instead. The authors of [33] modify the problem, and train a GC on features previously extracted by standard feed-forward network. For all these works, the most complex dataset used is CIFAR-100, at a resolution of 32×32 pixels.

So-called hybrid models [40] have been more successful in practice. Here, a likelihood estimation method is involved, commonly for the marginal $p(\text{image})$, while the actual classification is still performed in a discriminative way, using shared features between the two tasks. Notable examples are [31, 15, 11, 36, 21]. While these models can perform OoD detection, their main motivation has been semi-supervised learning. Hybrid models have some fundamental differences to GCs, e.g. that the conditional likelihoods are not directly modeled, and the latent space has no explicit class structure.

Concerning OoD detection with generative models, the authors of [35] observed that likelihood models trained on natural images are unsuitable for detecting certain types of OoD inputs, and may perform significantly worse than ran-

dom. This problem is addressed e.g. in [37, 10], where different OoD metrics are introduced that correct for these shortcomings. These works only consider unconditional likelihood models for OoD detection, while a separate classifier is still needed to perform the actual task. This means it is harder for the class content to factor in to both OoD detection and explainability techniques. GCs combine both these steps into a single model, potentially simplifying the process.

Adversarial attacks viewed as OoD data, specifically in relation to GCs, have also been addressed recently [43, 18, 34]. All three works use variational models as GCs which are shown to be more robust against adversarial attacks and able to detect them. While these works highlight the potential of GCs, they are limited to simple datasets, such as MNIST and SVHN. We want to investigate whether this observed behaviour extends to more complex tasks.

3. Methods

3.1. Invertible Neural Networks

While VAEs have been used as generative classifiers with some success [43, 18, 34], perhaps the most natural choice are normalizing flows, due to their exact likelihood estimation capabilities [14]. The networks used in normalizing flows are so-called invertible neural networks (INNs), a class of neural network architectures that meet the following conditions: (i) the network represents a diffeomorphism by construction (essentially, a smooth and invertible function), (ii) the inversion is computationally efficient to compute, and (iii) the network has a tractable Jacobian determinant. These conditions place some restrictions on the architecture, e.g. that the number of input and output dimensions have to be equal, and that non-invertible operations such as max-pooling can not be used. In recent years, various different invertible architectures have been developed that fulfill these conditions [13, 14, 4, 20]. In this work, we employ the affine coupling block architecture proposed in [14], with additional modifications, as described in Appendix A. When such coupling block INNs are trained in the same way as standard feed-forward networks, they only have a small disadvantage in terms of quantitative performance compared to standard architectures, despite the design limitations [29].

As mentioned above, the most popular application of INNs, that has driven much of the research in the past, are so-called normalizing flows. In any generative setting, there are training images X , that follow some unknown image distribution $p(X)$. The goal is then to approximate $p(X)$ as closely as possible with a distribution given by the network, which we denote as $q_\theta(X)$. In the case of normalizing flows, $q_\theta(X)$ is represented by transforming possible inputs X to a latent space Z using an INN f_θ ('flow'), with a prescribed standard normal latent distribution $p(Z) = \mathcal{N}(0, 1)$

(‘normalizing’). Then, the change-of-variables formula can be used to compute $q_\theta(X)$ at any point x through

$$q_\theta(x) = p(Z = f_\theta(x)) |\det J(x)| \quad (1)$$

with $J \equiv \partial f_\theta / \partial X$ being the Jacobian. It can be shown that the network will learn the true distribution ($q_\theta(X) = p(X)$) by maximizing the expected log-likelihood $\log q_\theta(X)$, as given through Eq. 1 above [48]. After training is complete, the model can not only be used to estimate likelihoods $q_\theta(X)$, but also to generate new samples by inverting the network, in order to map sampled instances of Z back to image space.

Class Conditioning In our case, this approach is not sufficient, as we want to use the INN as a generative classifier, meaning we need to model conditional likelihoods $q_\theta(X | Y)$. While different approaches for this exist [53, 2], we adopt the form introduced in [27]. Here, the latent distribution is a conditional density $p(Z | Y)$: The standard normal distribution $p(Z)$ is replaced with a Gaussian Mixture Model (GMM) containing a unit-variance mixture component per class

$$p(Z | Y) = \mathcal{N}(Z; \mu_Y, \mathbb{I}) \quad (2)$$

$$p(Z) = \sum_y p(y) p(Z | y) = \sum_y p(y) \mathcal{N}(Z; \mu_y, \mathbb{I}) \quad (3)$$

where μ_y is the mean of class y ; and the mixture weights are the class priors $p(y)$, i.e. the frequency of occurrence of each class in the dataset. The conditional likelihood $q_\theta(X | Y)$ can be evaluated with the change-of-variables formula (Eq. 1) as before by replacing the full distribution $p(Z)$ with the appropriate mixture component:

$$q_\theta(X | Y) = p(Z = f_\theta(X) | Y) |\det J|. \quad (4)$$

3.2. Training INNs with Information Bottleneck

Naively training such an INN with a class-conditional log-likelihood loss will generally not work, as the resulting models perform very poorly [17], even on only mildly challenging tasks. Instead, we require a loss function where the focus on the generative and class-separating capabilities can be explicitly adjusted and controlled. For this, we utilize the IB objective [50], which describes the ideal loss function for robust classification, from an information theoretical point of view. Given some features Z of a network, inputs X , and ground-truth task outputs Y , the IB loss consists of two terms using the mutual information I (MI):

$$\mathcal{L}_{\text{IB}} = I(X, Z) - \hat{\beta} I(Y, Z). \quad (5)$$

Intuitively, the MI measures the degree of shared information between variables, and can be written as the KL-divergence between the joint and factored distributions of

the variables:

$$I(V, W) = D_{\text{KL}}(p(V, W) \| p(V)p(W)), \quad (6)$$

By minimizing the IB loss, the amount of information about the desired output Y contained in the features $I(Y, Z)$ is being maximized. Simultaneously, the amount of information about the original input image contained in the features $I(X, Z)$ is minimized, which results in robust and efficient representations Z . The loss as a whole therefore yields a model which is as robust as possible while working at a given level of task performance. Furthermore, this trade-off can be explicitly adjusted by choosing $\hat{\beta}$.

How to apply this objective to INNs as GCs is not immediately obvious, as INNs preserve information, and the loss becomes ill-defined. The authors of [3] show that this can be avoided by adding very low noise to the inputs. This is mostly a formal requirement, as dequantization noise is used as a data augmentation for standard normalizing flows regardless. From this, the authors go on to derive two loss terms representing the IB objective, $\mathcal{L}_{\text{IB}} = \mathcal{L}_X + \beta \mathcal{L}_Y$. In practice, for our model, the two terms amount to the following, noting that $z = f(x)$:

$$\begin{aligned} \mathcal{L}_X(x) = & -\log |\det J(x)| \\ & + \frac{1}{2} \log \text{sumexp}_{y'} \left(\|f(x) - \mu_{y'}\|^2 - 2w_{y'} \right) \end{aligned} \quad (7)$$

$$\begin{aligned} \mathcal{L}_Y(x, y) = & \text{onehot}(y) \\ & \cdot \log \text{softmax}_{y'} \left(\frac{1}{2} \|f(x) - \mu_{y'}\|^2 - w_{y'} \right) \end{aligned} \quad (8)$$

Hereby, y' denotes the summation over all classes in the logsumexp and log softmax operations. The relative log-class weights $w_y := \log p(y)$ are usually learned, but for ImageNet we assume a constant $w_y = \log(1/(\# \text{ classes})) = \log(1/1000)$, making all classes equally likely. The difference between $\hat{\beta}$ in the original IB and β in the loss is a constant weighting factor, that makes both loss terms the same size at $\beta \approx 1$. More details can be found in [3].

Intuitively, we find the following: The \mathcal{L}_X -loss forces the data to follow the GMM in latent space. However, it has no effect on the class-conditional aspect, as the class y is summed out; note that the ground truth class is not used in the loss at all. This loss can be rearranged to look similar to the maximum-likelihood-loss used for normalizing flows, but with a GMM as a latent distribution. On the other hand, the \mathcal{L}_Y -loss bears resemblance to the categorical cross entropy loss, except that the usual logits are replaced by $\log p(z|y)p(y) = \log p(z, y)$. Therefore, \mathcal{L}_Y is responsible to make the likelihood model conditional on the class, but otherwise ignores the generative performance.

The trade-off parameter β determines how much the model focuses on capturing the class structure at high β

(important for classification performance, \mathcal{L}_Y), vs. modeling natural images at low β (important for generative performance, robustness, \mathcal{L}_X). In the limit cases, at $\beta \rightarrow 0$ we get a model which best models the training data distribution but ignores the class content. It will be maximally ‘robust’ in a sense, by always making useless random predictions. At $\beta \rightarrow \infty$, we have a model that can predict the class content of the input data, but we expect no generative capabilities, and the least robustness. We find that the trade-off is more nuanced in reality, as shown later in Sec. 4.1.

3.3. Detecting OoD Inputs

For likelihood-based generative models, OoD inputs are easily detected by directly utilizing the estimated probability density q_θ : in principle, if an input is outside the support of the training data, and the model has learned the true distribution, the OoD sample should be assigned $\log q_\theta(x) = -\infty$. In practice, it is only required that OoD samples have lower likelihood scores than the training data, so a threshold can be set. Any input with an inferred likelihood below this threshold is then treated as OoD (see Fig. 2, top). However, in [35], the authors identified various special cases where OoD inputs have an unnaturally high log-likelihood score. This prompted the development of a *typicality test* in [37], that uses both an upper and a lower threshold, centered symmetrically around the mean log-likelihood of the training data (Fig. 2, middle). For our ImageNet models, we observe that the distribution of log-likelihood values in the training set is highly asymmetrical. Therefore, we introduce a third possibility, a two-tailed quantile test. Instead of the thresholds being symmetric around the mean, they are chosen so that an equal mass of the log-likelihood histogram lies above the upper and below the lower threshold (Fig. 2, middle). In practice, we only measure minor differences in performance between the single-sample typicality test and the two-tailed quantile test.

All three tests can also be seen as hypothesis tests, with the null hypothesis being that the input is in-distribution. The p -value for the hypothesis test is the fraction of training samples with scores in the OoD-zone, which also equals the false positive rate. To evaluate the OoD detection capabilities, we do not use a single threshold value, but want a measure that is independent of it. This is because the acceptable false negative/false positive trade-off depends on the context/application that the model is used in. By varying the p -value of the test, we produce a receiver operating characteristic (ROC) curve. The area under this curve (ROC-AUC), in percent, serves as a scalar measurement of the OoD detection capabilities. An ROC-AUC of 100% means that the OoD samples are perfectly separated from the in-distribution samples and can always be identified correctly. A value of 50% indicates that the test performs exactly as well as randomly deciding. Below 50%, worse than

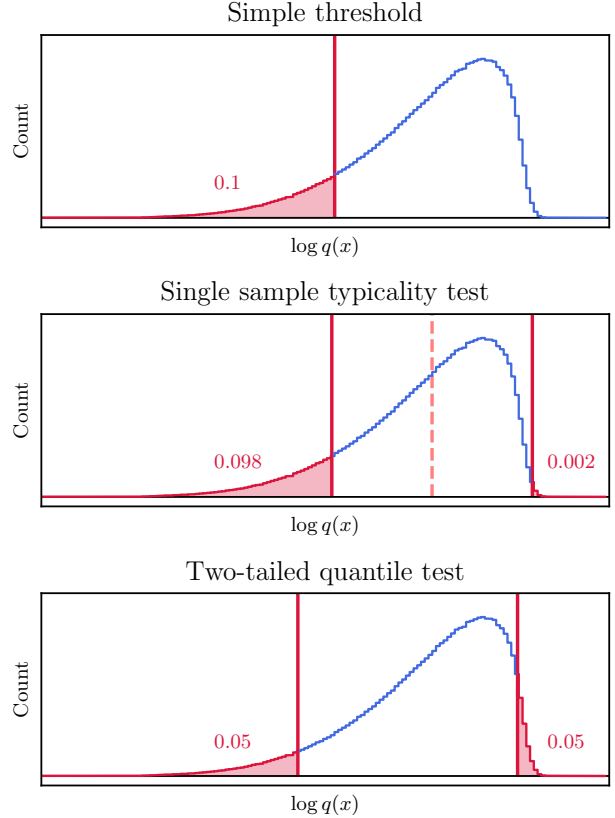


Figure 2: Illustration of three different OoD tests based on the estimated likelihood. The curve shows the distribution of likelihood scores in the training set. The blue part counts as in-distribution, and the red part as OoD. The threshold is chosen such that the red area (false positive rate, p -value), is 0.1 in all three cases, for illustration. In practice, this would be chosen much lower, e.g. 0.001. The small red numbers indicate the fraction of training samples above and below each threshold.

random performance, the OoD data appears to be more in-distribution as a significant fraction of the training data itself.

4. Experiments

4.1. Network Architecture

A detailed description of the network architecture is found in Appendix A, we summarize the main points in the following.

We construct the invertible network (INN) from affine coupling blocks, as introduced in [14], with various modifications from other recent works [1, 2, 28, 30]. As invertible alternatives to 2×2 max-pooling and global mean-pooling, we use a Haar wavelet transform [2] and a DCT transform

Layer	Blocks	Im. size	Channels		R.F.	
			INN	ResNet	INN	ResNet
Input		224	3	3		
Entry flow	1	112	12	64	8	6
Pool (Haar/max)		56	48	64	10	10
Conv_2.x	3	56	48	256	34	34
Conv_3.x	4	28	192	512	106	90
Conv_4.x	6	14	768	1024	314	266
Conv_5.x	3	7	3072	2048	538	426
Pool (DCT/avg.)		1	150528	2048	∞	∞

Table 1: For each of the resolution levels in the INN and ResNet-50, the number of coupling/residual blocks and spatial size is given, along with the number of feature channels and the maximum possible receptive field (R.F.).

	ResNet	INN
Network parameters (M)	23.5	55.4
All parameters (M)	25.6	77.5
FLOPs (G)	4.07	9.08

Table 2: Number of parameters and computational cost for each model. ‘*Network parameters*’ only counts the coupling/residual blocks. ‘*All parameters*’ additionally includes the fully connected output layer of the ResNet, and the parametrization of μ_y for the INN. The (M) and (G) indicates Mega and Giga respectively. For FLOPs, the fused multiply-add instruction (FMA) is counted as a single FLOP, as it is commonly a single instruction in modern computing architectures.

[28] respectively.

Because of the similarities between affine coupling blocks and residual blocks used in a ResNet, we match the design of the INN to that of a standard ResNet-50 wherever possible. The overall layout is summarized in Table 1, c.f. [22], Table 1. Some differences arise due to the constraint of invertibility: the number of feature channels and the available receptive field vary between the two networks.

The invertibility is associated with an extra cost of parameters and computation cost. Table 2 summarizes this in comparison to a standard ResNet-50. Both in terms of network parameters, as well FLOPs needed for one forward pass of the network, the cost of the INN is about twice as high as the ResNet. We are optimistic this overhead can be reduced in the future with more efficient INN architectures.

4.2. General Performance

Losses and task performance. We train several generative classifiers, with values of the hyperparameter $\beta \in \{1, 2, 4, 8, 16, 32, \infty\}$, while all other hyperparameters stay constant. To reiterate: β controls how much the model focuses on the generative likelihood estimation aspect (low β), vs. prioritizing good classification performance (high

β	$\mathcal{L}_X^{(\text{test})} (\downarrow)$	$\mathcal{L}_Y^{(\text{test})} (\downarrow)$	Bits/dim. (\downarrow)	Acc. (%) (\uparrow)
1	-1.90	8.52	4.34	67.30
2	-0.65	8.26	6.14	71.73
4	1.14	8.14	8.72	73.69
8	3.66	8.10	12.35	74.59
16	7.17	8.06	17.43	75.54
32	10.81	8.01	22.68	76.18
∞	27.68	7.99	47.01	76.27
0	-3.11	—	2.59	—
ResNet	—	7.87	—	77.40

Table 3: Test losses and metrics for models trained with different β . Bits per dimension is the most commonly used metric to evaluate the performance of density estimation models, see text. As with the original ResNet, the accuracy is computed using 10-crop testing.

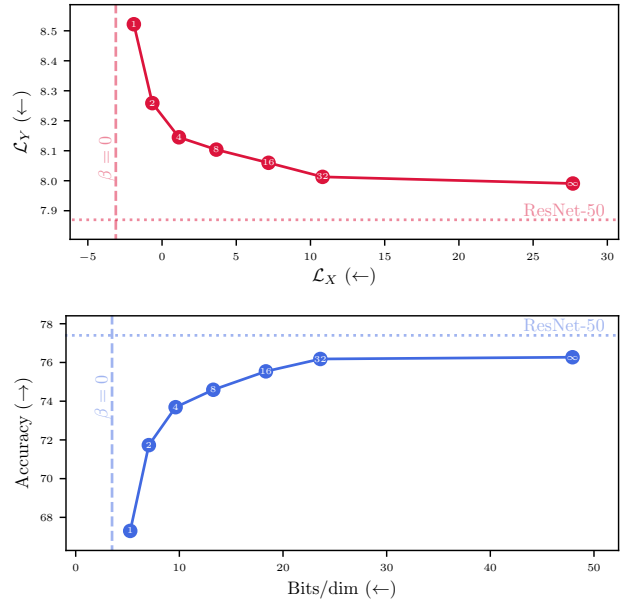


Figure 3: Trade of between the two losses \mathcal{L}_X and \mathcal{L}_Y (top), and between generative modeling accuracy in bits/dim, and top-1 accuracy (bottom). Each point represents one model, trained with a different beta. A standard ResNet has no \mathcal{L}_X loss, and is shown as a horizontal line, and the model with $\beta = 0$ (standard normalizing flow) is missing the \mathcal{L}_Y loss, and is shown as a vertical line. The small white numbers inside the markers give the value of β of that particular model.

β). We use these models throughout the experiments, to examine the differences between GCs and DCs in a continuous way. In addition, we include a model trained with $\beta = 0$, i.e. no classification at all, analogous to a standard normalizing flow, as well as a standard feed-forward ResNet-50 [22].

The primary performance metrics used in Table 3 and Fig. 3 are firstly, the top-1 accuracy on the test set (in our case, the ILSVCR 2012 validation set [42]), using 10-crop testing. In detail, the image is resized so the shortest edge is 256 pixels, and then cropped to a square. Next, five 224×224 -pixel patches are cropped from the corners and center, as well as their horizontally flipped versions, giving 10 crops in total. Finally, each of these 10 crops is passed through the network, and the logits are averaged before the final softmax operation. This is the method used most often for this setting, so we adhere to this standard. For a generative classifier, as there are no logits per se, the logit averaging is analogous to taking the geometric mean over the 10 input crops for both the denominator and numerator of Bayes rule.

Secondly, for the generative likelihood estimation performance, we use the bits per dimension (*'bits/dim'*) metric, as this is the prevalent evaluation metric for such models. It quantitatively measures the accuracy of the likelihood estimation. Originating in models that estimate the density on discrete inputs (e.g. 255 brightness levels per RGB channel per pixel [39]), bits/dim measures how many bits would be needed on average to store the value of each input dimension, if an ideal encoding were formulated using the models estimated likelihoods. If the quality of the likelihoods is worse, the encoding will be less efficient w.r.t. to the real data, and more bits will be needed to store the inputs. This can be generalized for continuous density models such as standard normalizing flows, explained e.g. in [49]. Importantly, it can be shown that bits/dim is exactly proportional to the KL-divergence between the true and estimated densities:

$$\text{bits/dim} \propto D_{\text{KL}}(p(X) \parallel q_{\theta}(X)) + \text{const.} \quad (9)$$

However, the constant offset is fundamentally unknown and data dependent, so while bits/dim is a strong quantitative metric to compare different models against each other, it cannot indicate how good the model is on an absolute level.

In Table 3, we report the test losses and the two discussed performance metrics for the different models. Further shown in Fig. 3, changing β moves smoothly between the limit cases of a feed-forward network, and a pure density estimation model: the classification accuracy increases continuously with β , but a minor gap remains to the feed-forward ResNet-50, in line with works such as [29]. At the same time, the bits/dim grows continually worse compared to the purely generative model ($\beta = 0$).

Receptive field. While the maximum possible receptive field (RF) of the INN and a standard trained ResNet are roughly comparable (see Table 1), we see large differences in the effective RF. For the effective RF, we pick a feature

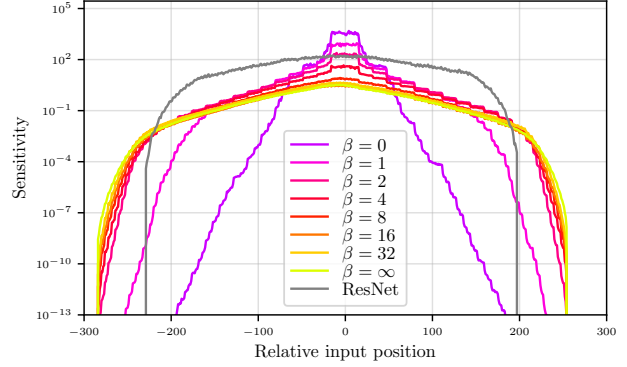


Figure 4: Effective receptive field for each value of β , just before the final pooling operation. Note the logarithmic sensitivity axis.

space column u , before the DCT pooling operation. Meaning, from the $H \times W \times 3072$ feature space, u will be the $1 \times 1 \times 3072$ column. We choose a column from the center to avoid interactions with the edges. We call the individual features u_l ($l = 1 \dots 3072$). We now measure the gradient w.r.t. each channel of each image pixel x_{ijk} , for real input images. The pixel position is ij , and the color channel is k . We define the ‘sensitivity’ of the model at each position as the L_1 norm of the gradient of the features w.r.t. that input position, averaged over images from the test set:

$$\text{Sensitivity}(i, j) = \mathbb{E}_{x \in \text{test}} \left[\sum_{k=1}^3 \sum_{l=1}^{3072} \left| \frac{\partial u_l}{\partial x_{ijk}} \right| \right] \quad (10)$$

There are other definitions that would be equally sensible (squared gradients, frobenius norm, etc.), but the results always show the same behaviour.

The cross-sectional shape of this represents the effective RF, and is shown in Fig. 4. We observe that for low β , the effective RF is very narrow. In fact it is almost as narrow as it could possibly be: for $\beta \leq 4$, the FWHM of the sensitivity is only 64 pixels. This is the same we would get from only the downsampling steps, without any spatial convolutions (with 6 downsamplings, $2^6 = 64$). This could indicate that for the likelihood estimation, local details and structures are more important than any long-range features. For higher values of β , the response more closely matches that of a standard trained ResNet (1.25 times wider in line with the 1.25 times larger maximum possible RF).

Calibration The calibration of a model measures the truthfulness of the predictive posteriors. In short, if we consider predictions where the model is e.g. 80% confident in a class, we would expect the prediction to be correct 80% of the time. If it were correct more often, it would be under-confident, and vice versa, more commonly, if it were correct

	1.0	2.0	4.0	β				RN
ECE (%)	0.16	0.16	0.16	0.17	0.16	0.17	0.17	0.17
MCE (%)	5.54	3.13	5.47	4.57	5.50	5.28	5.10	7.72
OCE	3.87	4.13	4.31	4.73	4.15	4.94	5.12	6.75

Table 4: Calibration Errors for different values for β and for the ResNet. Expected Calibration Error (ECE), Max Calibration Error (MCE), Overconfidence Calibration Error (OCE)

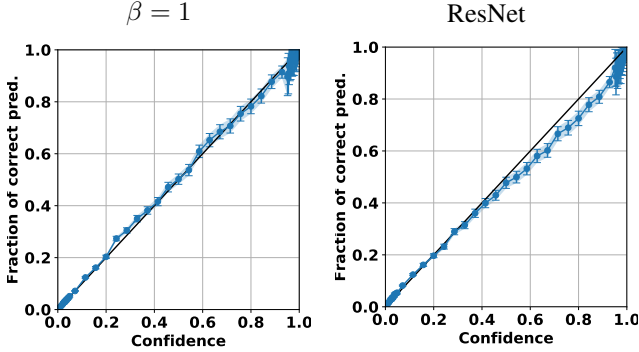


Figure 5: Calibration curves for the model with $\beta = 1$, and a standard ResNet-50, for reference. Deviations below diagonal = overconfidence, above = underconfidence. The error bars are the Poisson errors computed from the bin count.

in much fewer than 80% of cases, it would be overconfident. Plotting the fraction of correct predictions R over the binned confidence C of predictions gives the so-called calibration curve $R(C)$. For a perfectly calibrated model, the curve will follow the diagonal, but usually the behaviour deviates.

To quantitatively measure the deviations, we compute the expected- (ECE), the max- (MCE) and the overconfidence calibration error (OCE). More details on the computation of these measures can be found e.g. in Appendix D of [3]. The ECE measures the expected distance from the diagonal, weighted by the bin count $n(C)$ at any confidence:

$$\text{ECE} = \frac{1}{n_{\text{tot}}} \sum_C n(C) |C - R(C)| \quad (11)$$

But for tasks with more than ~ 10 classes, the ECE is almost completely dominated by the ‘negative’ predictions: for any ImageNet prediction, typically only a few classes have a meaningful confidence, while e.g. 990 of the 1000 classes will have confidences $< 0.1\%$. So the lower end of the curve is weighted ~ 100 times stronger than the rest of the curve, severely shifting the ECE statistic towards the very low confidence regime. The MCE measures the maxi-

mum distance from the diagonal:

$$\text{MCE} = \max_C |C - R(C)| \quad (12)$$

The MCE is not affected by the same phenomenon as the ECE, but in return is subject to random fluctuations of sparsely populated regions on the curve; it only takes a single bin into account. Finally, the OCE measures the normalized fraction of wrong predictions that are highly confident with $C \geq C_{\text{crit}}$, where we use $C_{\text{crit}} = 99.7\%$.

$$\text{OCE} = \frac{1}{1 - C_{\text{crit}}} \sum_{C \geq C_{\text{crit}}} |1 - R(C)| \quad (13)$$

For instance, an OCE of 3.5 would mean that in these high-confidence cases, the model is wrong 3.5 times more often than allowed, the error rate should be $\leq 1 - C_{\text{crit}} = 0.3\%$ in these cases. This measures more directly the cases we may be interested in: we want to be able to trust the decisions if they are very confident. The OCE is less noisy than MCE in our case, as it takes more samples into account.

We report the result in Table 4. The full calibration curves for all considered classifiers can be found in Appendix Fig. 20. In short, we confirm previous observations e.g. in [3]: the GC models are better calibrated than DCs. The OCE shows the clearest trend of increasing overconfidence with β . Even from the $\beta = \infty$ model to the standard ResNet, there is a significant jump in the calibration error, also seen clearly in the full calibration curves. As the loss function for training at $\beta = \infty$ is essentially the same as a standard ResNet, this must be due to the construction of the model. Explained further in 4.3.2, our conjecture is that it is due to the latent space structure specifically.

4.3. Explainability

We do not perform an exhaustive analysis and comparison of all possible explainability techniques, this far exceeds the scope of a single paper. Furthermore, the quality of an explanation is highly subjective, and also depends on the context the model is used in. In the following, we simply demonstrate several examples how GCs can be used for native and intuitive explanations of the data and the prediction outputs. Certainly, algorithms and approaches exist that can generate similar results for DCs. The point made by the following examples is simply that various explanations are accessible using only the structure of latent space and the learned likelihoods, without requiring many additional modifications or heuristics.

4.3.1 Visualizing decision-space

The properties of a classification decision can in principle be easily seen, by passing an input image through the network, and observing its position in latent space in relation

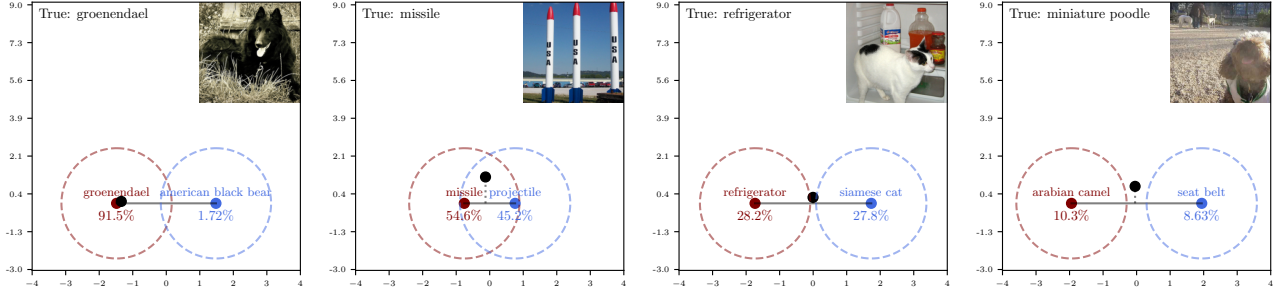


Figure 6: Latent space location of input images (*black point*) in the decision space spanned by the μ_y of the top 5 predicted classes. The horizontal axis of the plot is the axis connecting the the top 2 predicted classes (*red and blue points*). The vertical axis of the plot shows the radial distance from the horizontal axis in the 5D space. The illustrative circles are chosen such that in both the vertical and horizontal directions, 90% of the mass of the Gaussian mixture component lies inside. Note that the axes in the plot are scaled differently to make it appear as a circle. From left to right: Confident in-distribution decision, uncertain in-distribution decision due to ambiguous classes, uncertain decision with unambiguous classes, uncertain out-of-distribution decision.

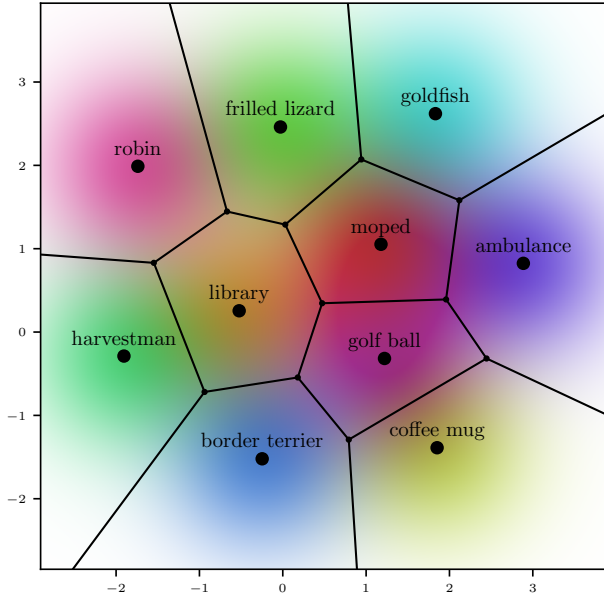


Figure 7: Latent space of a model with only ten classes, where the μ_y (black points) are constrained to a plane. The black lines are the decision boundaries, e.g. all points inside the ‘moped’-polygon will be classified as a moped. The background is colored according to the probability density of each mixture component.

to the surrounding classes. The only difficulty consists in plotting the high-dimensional vectors in a 2D figure.

One possibility how this can be done is shown in Fig. 6. First, for the latent vector of a given input, the five closest class centers μ_y are found. By construction, this will also be the top 5 predicted classes. The latent vector is then

projected to the subspace spanned by these classes. The decision process is almost entirely determined by what happens in this subspace, as the remaining 995 classes typically make up $< 1\%$ of the total predicted probability. From here, the horizontal axis of the 2D plot is the line connecting the top two classes, and the vertical simply gives the radial distance to the other three classes orthogonal to this connecting line. Examples for several different inputs are shown in Fig. 6.

A second method is shown in Fig. 7. Hereby, the task is simplified to allow for a 2D visualization: A subset of 10 ImageNet classes is selected. Starting from the full model, the μ_y of the selected classes are constrained to a plane and fine tuned, reaching 90% accuracy for this simplified 10-class case. This allows us to show the entire decision space in a single 2D plot. The decision boundaries between all classes form a Voronoi tessellation of the decision space. All latent vectors inside the Voronoi cell of a certain class will have the highest probability under that class. In the case where the μ_y are not constrained to a plane and all 1000 classes are used, the behaviour is the same, with high-dimensional polygons for each class, but this can not be readily visualized.

4.3.2 Class similarities

Building on the previous example, we see that different classes have various amounts of overlap. We can examine this more closely, as it pertains to the relative relationships between classes. This is not possible for a feed-forward model, as there is no latent space where the input data is embedded in such a way. We observe that the locations μ_y of the Gaussian mixture components are close together for classes that are semantically similar, and far apart for

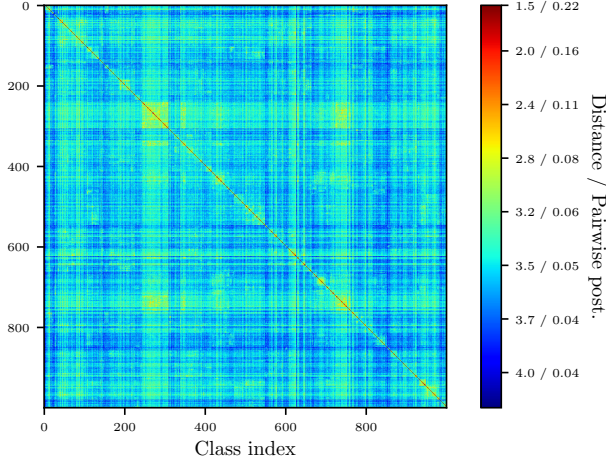


Figure 8: Similarity matrix between all 1000 classes. The two large clusters around class index 250 and 750 are dogs. The colormap indicates the pairwise distance of the μ_y as well as the expected pairwise posterior, meaning e.g. the binary decision between a tabby cat and a tiger cat is associated with 20% expected uncertainty, by construction (see text).

classes that are dissimilar.

Importantly, this also has implications for the predictions the model makes. For instance, in Fig. 6, 2nd from left, the classes overlap a lot. This means more points will lie in the overlap zone, and consequently more of these decisions will be uncertain, compared to e.g. the 3rd from the left, where most inputs will be in only one of two classes. More precisely, the closer two class centers are, the larger the overlap is, and the larger the proportion of decisions between these two classes that will be uncertain. In fact, for two classes A and B, if A is the top prediction, the expected posterior for class B can be worked out explicitly from the distance between the μ_A and μ_B in latent space, see Appendix B. We do this pairwise for all 1000 classes, with the results seen in Fig. 8.

These considerations highlight an important fact: the latent mixture model contains a built-in uncertainty between classes. A decision between similar classes will always be uncertain, by the structure of latent space alone, not fully reliant on the actual model outputs. This may be one of the factors explaining why the predictive uncertainties are overall better calibrated in such GCs [3].

4.3.3 Heatmaps and saliency-maps

To increase the trust in a decision, it is often helpful to show which regions of the image were relevant. Examples are widespread where models e.g. base the decision on the background of the image, not the object in question, or fo-

cus only on a specific detail that identifies an object. Approaches such as CAM or GradCAM [56, 44] are used to generate coarse heatmaps showing regions that are influential for a particular decision. For the INN-based generative classifier, we can replicate such heatmaps. Interestingly, they can be written as a direct decomposition of the prediction output, so the heatmaps can be more understood as simply a different way of representing the actual model output, rather than a post-hoc explanation technique.

To produce a spatially structured output, we consider the following: Due to the invertibility of every part of the model, we can start from the output z , and transform it back through the DCT operation. Unlike standard mean-pooling, the DCT pooling does not lose any information in either direction. We define the following for short:

$$\begin{aligned} w^{(y)} &= \text{DCT}^{-1}(z) - \text{DCT}^{-1}(\mu_y) \\ &= \text{DCT}^{-1}(z - \mu_y). \end{aligned} \quad (14)$$

Because the DCT operation is linear and orthogonal, it conserves distances, and we can write

$$p(z|y) \propto \exp\left(-\frac{1}{2}\|z - \mu_y\|^2\right) = \exp\left(-\frac{1}{2}\|w^{(y)}\|^2\right) \quad (15)$$

We can consider the spatial structure present in $w^{(y)}$: It will have three indices, k, l for the spatial position and m for the feature channels: $w_{klm}^{(y)}$. We can simply factorize over the spatial dimensions. For the log-probability, we get

$$\log p(z|y) = \sum_{k,l} -\frac{1}{2}\|w_{kl,:}^{(y)}\|^2 + \text{const.} \quad (16)$$

$$:= \sum \log p(w_{kl}|y) \quad (17)$$

We can now consider the class prediction:

$$q_\theta(y|x) = \frac{p(z|y)}{\sum_{y'} p(z|y')} =: \frac{p(z|z)}{S(z)}, \quad (18)$$

where $p(y) = 1/M$ and the Jacobian $|\det J|$ both cancel out. We therefore plot for any class the following ‘class posterior heatmap’:

$$Q_{\text{Class}}(k, l, y) = \log p(w_{kl}|y) - S_{kl} \quad \text{s.t.} \quad \sum_{kl} S_{kl} = S \quad (19)$$

The $-S_{kl}$ term means a fixed ‘image’ is subtracted from each heatmap, representing the denominator, which is constant for all classes. There is some freedom to choose S_{kl} , as long as it sums to S . When distributing it evenly over space, the differences in the heatmaps between classes are hard to see by eye, compared to the common differences within the heatmaps shared across classes, which are larger

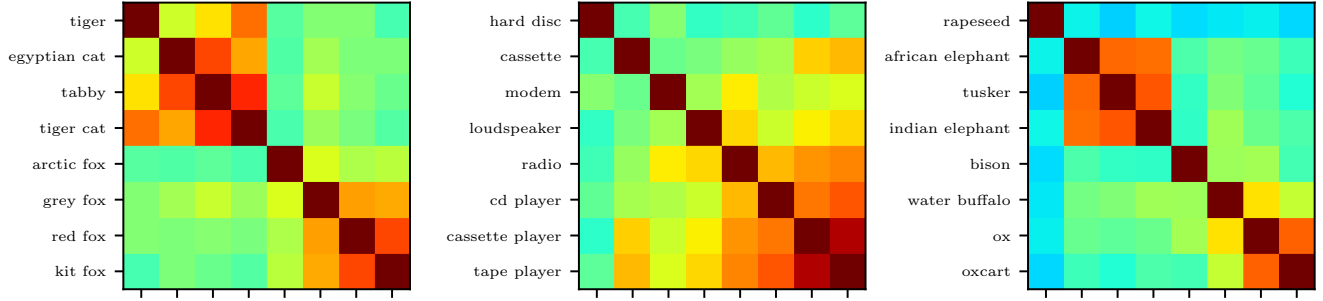


Figure 9: Magnified regions of the similarity matrix in Fig. 8, using the same colormap. The distance on the diagonal is 0 (outside colormap range).

by magnitude. Heuristically, we instead find the best contrast when we choose the relative weight of each S_{kl} in the following way:

$$S_{kl} = S \frac{r_{kl} + 0.03}{\sum_{kl} (r_{kl} + 0.03)} \quad (20)$$

where r_{kl} is the same as $\log p(w_{kl})$ but normalized to the $[0, 1]$ -range over each image. Some examples are shown in Fig. 10.

Comparing to Eq. 18, we see that summing Q_{Class} over feature-space pixels gives exactly the log-prediction $\log q_{\theta}(y|x)$. So Q_{Class} represents a spatial decomposition of the actual predictive output:

$$q_{\theta}(y|x) = \exp \left(\sum_{kl} Q_{\text{Class}}(k, l, y) \right) \quad (21)$$

4.4. Measuring Robustness

In current literature, there is no agreement upon a single measurement that clearly defines robustness in deep learning. In general, the question is how a model reacts to out-of-distribution (OoD) inputs, meaning inputs that do not come from the same distribution as the training data. OoD data can be further categorized, among others: Images from a slightly different (‘shifted’) data distribution, e.g. synthetic training and real test images; images which were once in-distribution, but which are corrupted in some way; images that are semantically unrelated to the training data and/or show specific objects that have never been observed before; and images that are maliciously altered to trick the model, so-called adversarial attacks. In the following, we briefly discuss four different measurements that can all be understood to quantify robustness.

In the case that the OoD data semantically contains the same information as the training data, especially for dataset



Figure 10: Examples of the prediction heatmaps. Top: bowtie and sunglasses are located, suit is distributed over a large area. Middle: The head of the bird causes it to be classified as a limpkin, whereas the feathers are more indicative of an eagle of vulture. Bottom: The heatmaps of both Rottweiler and Appenzeller classes are located in the same area (ambiguous classes), while the soccer ball is separate.

shifts, the most straight forward understanding of robustness is that the model **retains good performance** for these OoD inputs. Measuring this is easy, it simply means measuring the task performance on OoD data and comparing to the performance on in-distribution test data. But there are other cases where this definition is not applicable or realistic: There is no ‘correct’ prediction if the OoD input does not contain one of the classes that was trained for, or if the image is completely corrupted and semantically unrecog-

nizable.

A second idea of robustness is therefore, that the model should at least make **uncertain predictions** for OoD inputs. In reality, standard (non-robust) models make highly overconfident predictions on OoD data [45]. The most direct measure of this is the discrete entropy of the predictive outputs, as discussed in [45].

Thirdly, a robust model can be one that is able to **explicitly detect** OoD inputs. In this case, along with the usual task output, the model has some auxiliary output that indicates whether an input is OoD. The model is robust by explicitly indicating that it’s prediction may not be trusted in these cases. GCs are uniquely suited for this, as the estimated likelihood of the inputs can serve as a built-in OoD detection mechanism, but other approaches also exist [32, 25, 9]. To measure this, metrics such as the area under the receiver-operator curve can be used (AUC-ROC).

Finally, in the context of adversarial attacks, robustness is commonly understood to be the **amplitude of adversarial perturbation** necessary to trick the model [54]. If the adversarial perturbation is large enough, it is visible to humans and also easier to detect. This can be measured e.g. through the L_2 distance between the original and the attacked image.

4.5. Handling Corrupted Images

We first consider the robustness test established by [24]. Here, the existing ImageNet validation images are corrupted with 5 severity levels in 15 different ways, summarized in the categories: noise, blur, weather, and digital. The authors propose the mean corruption error (mCE) and the relative mean corruption error (rel. mCE) score to measure the robustness of a classifier. The mCE measures the error of some model f , weighted and then aggregated over all corruptions. The weight is computed based on the achieved error of the AlexNet classifier on the different corruptions as different corruptions pose different levels of difficulty. The measure is computed as follows

$$\text{mCE}^f = \frac{1}{15} \sum_{c=1}^{15} \frac{\sum_{s=1}^5 E_{s,c}^f}{\sum_{s=1}^5 E_{s,c}^{\text{AlexNet}}}, \quad (22)$$

with $E_{s,c}^f$ denoting the classification error of model f , given the corruption type c with the severity s . $E_{s,c}^{\text{AlexNet}}$ stands for the error achieved by AlexNet and is used as a weight of difficulty for a particular corruption c with severity s .

The relative mean corruption error instead measures the performance degradation of a classifier f relative to its performance on uncorrupted data. It is computed as follows

$$\text{Rel. mCE}^f = \frac{1}{15} \sum_{c=1}^{15} \frac{\sum_{s=1}^5 E_{s,c}^f - E_{\text{clean}}^f}{\sum_{s=1}^5 E_{s,c}^{\text{AlexNet}} - E_{\text{clean}}^{\text{AlexNet}}} \quad (23)$$

with E_{clean}^f and $E_{\text{clean}}^{\text{AlexNet}}$ standing for the errors achieved on the uncorrupted ImageNet validation set for classification model f and the AlexNet classifier respectively.

Again, we report all results obtained by our models and the ResNet. As can be seen in Table 5 our GCs do not show an increased robustness to the applied corruptions in terms of mCE. However, the GCs do infer less confident predictions on the corrupted images, compared to the DCs, seen from the predictive entropy. Furthermore, we are able to classify these images as outliers. Generally, we observe better OoD detection scores for smaller values for β . The *Snow*, *Frost* and *Brightness* corruptions remain hard to detect. We find the GC trained with $\beta = 2$ to be the most robust classification model: It is able to detect a wide range of corruption types while being a reasonably good classifier (4.54 percentage point classification performance gap compared to the $\beta = \infty$ model and 5.67 percentage point gap compared to ResNet). To summarize: The GC models are not more robust to synthetically applied corruptions in terms of task error. Some types of corruptions can be accurately detected, while others are not detected at all.

4.6. Handling Adversarial Attacks

We are interested in finding out if generative classifiers are more robust to adversarial attacks when using high dimensional data such as ImageNet. We are not proposing a new, competitive method of adversarial attack defense, the goal is simply to examine whether GCs are naturally more robust to adversarial attacks on ImageNet, in the same way it was observed for e.g. MNIST previously [34, 43].

For evaluation, we performed a well established white-box targeted attack method introduced by [8]. Here, the attacked image is parametrized as $x_{\text{att}} = \frac{1}{2}(\tanh(w) + 1)$, to ensure the image values are between 0 and 1. The attack then consists of optimizing w directly to minimize the following objective:

$$\begin{aligned} \mathcal{L}_{\text{CW}}(w, x) = & \|x_{\text{att}}(w) - x\|^2 \\ & + c \max \left(\max(\{l_y : y \neq t\}) - l_t, -\kappa \right) \end{aligned} \quad (24)$$

The original image is x , and the logits output by the model for each class y are l_y . The target class, that the attacked image is supposed to be classified as, is t . The logits are re-computed by the model on each iteration using the updated $x_{\text{att}}(w)$, which they depend on: $l_y = l_y(x_{\text{att}}(w))$. The gradients are propagated through the model.

In other words, the attack objective simultaneously attempts to make x_{att} and x the same, and to maximize the difference between the logit of the target class, and the currently next highest predicted class. Once the distance is larger than the hyperparameter κ in favour of the target

β	Clean Error	mCE	rel. mCE	Δ entrop.	OoD	Noise			Blur				Weather				Digital			
						Gauss.	Shot	Impulse	Defocus	Glass	Motion	Zoom	Snow	Frost	Fog	Bright	Contrast	Elastic	Pixel	JPEG
0	—	—	—	—	77.51	94.9	94.3	98.0	95.7	89.8	88.3	89.5	38.1	43.1	94.8	44.7	96.7	65.5	63.0	66.2
1	32.7	98.5	116	1.62	67.9	95.3	95.2	98.6	92.9	87.1	84.9	87.4	33.0	45.4	96.5	43.5	97.0	60.4	61.9	55.6
2	28.27	92.5	119	1.75	73.6	94.8	95.2	98.5	87.8	82.6	81.3	84.9	30.9	43.2	96.5	44.1	95.2	56.6	61.0	51.2
4	26.31	88.2	117	1.72	70.84	92.7	93.8	97.4	77.6	76.7	75.6	81.7	31.0	43.2	95.5	44.5	89.2	54.1	61.7	48.0
8	25.41	86.8	117	1.81	65.85	89.3	91.2	94.6	56.9	63.5	63.1	73.7	37.6	46.6	87.8	45.1	71.2	53.1	65.1	49.1
16	24.46	84.9	115	1.79	62.43	83.7	84.6	88.0	46.7	56.7	63.5	67.9	43.2	52.0	80.2	45.6	66.3	53.3	62.0	42.7
32	23.82	83.1	113	1.71	55.83	81.6	81.5	84.0	39.8	51.6	50.1	54.8	43.9	44.3	61.6	44.6	53.9	52.4	52.5	41.1
∞	23.73	83.4	114	1.58	44.24	39.5	44.5	40.6	42.8	48.1	46.3	46.0	40.9	38.9	36.1	44.3	48.5	52.2	47.9	47.0
ResNet	22.6	78.2	109	1.51	—	—	—	—	—	—	—	—	—	—	—	—	—	—	—	—

Table 5: We report the error obtained on the unperturbed images (*clean error*), the mean corruption error (*mCE*), the relative mean corruption error (relative performance degradation caused by the corruptions), the average difference in predictive uncertainty between corrupted and clean images (Δ *entrop.*), and the OoD ROC-AUC detection score (*OoD*) averaged over all types of perturbations as well as for the individual corruptions. Meaning of colors: **good detection** $\geq 85\%$; **some detection** $> 55\%$; **random or worse detection** $\leq 55\%$.

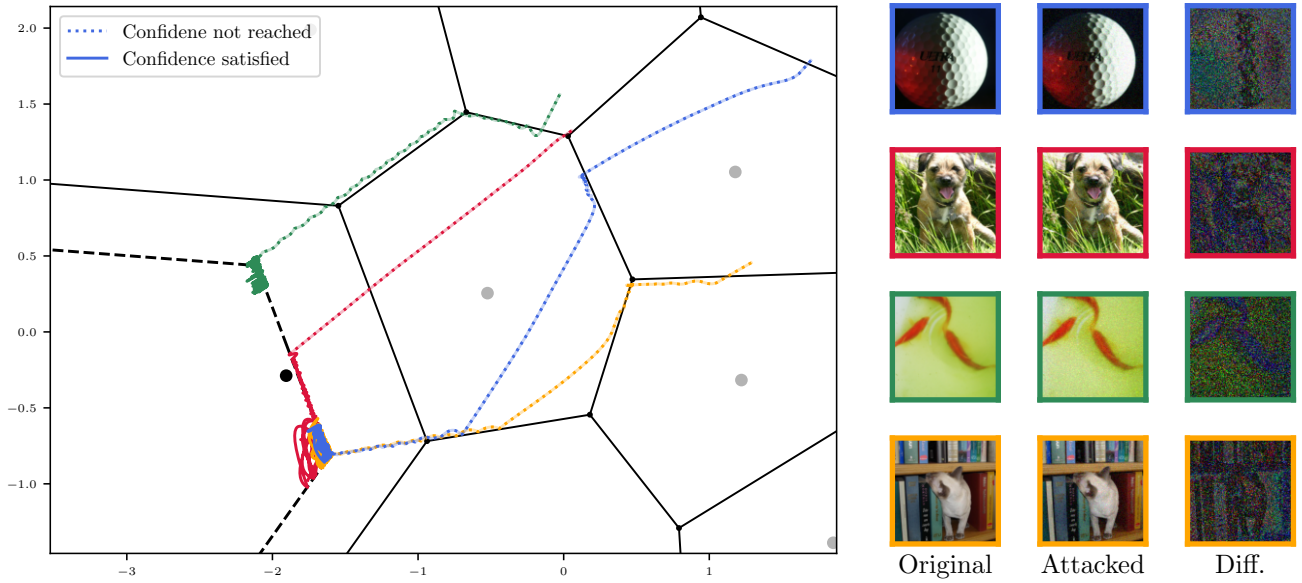


Figure 11: Trajectory of four adversarial attacks on the 10-class model from Fig. 7 shown in latent space (*colored curves*), with $\kappa = 1$, $d = 0$. In the dotted section of the curves, the classifier is not yet fooled with sufficiently high confidence. In the solid section, the classifier has been fooled, and the attack only tries to reduce the perturbation. The large black dot indicates the position of μ_{target} (the position with highest probability density for this class), the target class being ‘Harvestman (spider)’. The solid black lines are the decision boundaries to the surrounding classes. The dashed black lines are the boundaries of the region where the classifier is fooled with sufficiently high confidence corresponding to κ . On the right, the four attacked images are shown, along with the resulting perturbation. More examples given in Appendix C.

class, this loss term does not contribute anymore. Adjusting κ therefore has a direct influence on the confidence of the (wrong) predictive posterior. From an attackers point of view it is optimal to fool a classifier to make certain but wrong predictions by setting a high value for κ , while finding a w so that x_{att} is as close as possible to the original image x . Ideally the differences between x_{att} and x remain imperceptible to the human eye. From the victim networks point of view, the targeted wrong prediction should be as uncertain as possible, and the difference between x_{att} and

x as large as possible.

For GCs, there are not logits per se. Instead, we use the conditional log-likelihoods $l_y = \log p(x|y)$, to get the same behaviour. We performed all adversarial attacks on the same randomly chosen 200 test images, paired with the fixed random target class each. To perform the attack, we use the Adam optimizer with its initial learning rate set to 0.01, as in [8]. We performed the attacks with three different values for κ : 0.01, 1.0, ∞ . The parameter c was fixed and set to 10, which is the lowest possible value for achieving a 100%

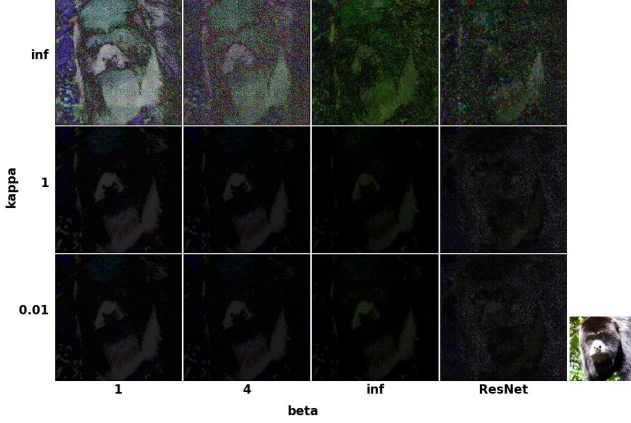


Figure 12: Qualitative results demonstrating the influence of κ (controlling the classifiers final confidence on targeted classes) and β (controlling the generative modeling capability of the classifier) on adversarial attack robustness. The discriminative classifier ResNet is added for reference. The figure, showing the per-pixel errors in RGB space, gives the absolute difference between the original (bottom right corner) and the adversarially perturbed image, amplified by a scaling factor for visibility. For adversarial attacks to achieve highly confident posteriors (high value for κ) the noise has to be amplified. In order to successfully trick a classifier with better generative modeling capabilities (low value for beta) the noise added by the attack has to be even larger.

attack success rate on all our tested models. We assume the attack converged whenever \mathcal{L}_{CW} stops improving for 20 consecutive gradient steps.

Explainable Adversarial Attacks In Fig. 11, we perform an attack on the model from Fig. 7. The trajectory of the attack in decision space can thus be visualized. We find that the attack consists of two distinct stages. First, the attack attempts to cross into the area belonging to the target class, leaving a certain margin specified implicitly by κ . Second, the attack minimizes the magnitude of the adversarial perturbation, while staying inside this region (sometimes stepping outside the region for a single iteration). More examples are given in Appendix C, Fig. 21. For the full model with 1000 classes, we see the same behaviour, although the decision boundaries can no longer be visualized (see Appendix C, Fig. 22). For the 2D figure, we consciously chose a target class located at the ‘edge’ of the latent space, not circled by other classes on all sides. This is because for the 1000 class case in higher dimensions, all classes are essentially guaranteed to be such ‘edge’ classes.

An important lesson to take from this, is that the area of maximal confidence of the attack is not necessarily closest

to μ_{target} . Instead, the confidence depends on the *difference* of the squared distance to the other classes (see Eq. 24). Especially for high κ , sufficient confidence is only achieved far outside of the original distribution. This facilitates reliable detection in these cases, see quantitative results below.

Quantitative Results All results concerning adversarial attacks are summarized in Fig. 13. We observe the GCs to be measurably more robust, in terms of necessary adversarial perturbation, growing with smaller β . The gap to the ResNet (roughly factor 2) is consistent to what was observed for a simplified version of CIFAR10 in [34, Fig. 7]. We would expect the trend to continue for $\beta < 1$, for the adversarial perturbations to be even larger, but at that point the task performance may not be satisfactory anymore. In terms of κ , the adversarial perturbations increase a lot for $\kappa = \infty$ (confident fooled predictions), but the increase is homogeneous across models including the ResNet. We show this qualitatively in Fig. 12. Furthermore, as can be seen in Figure 29 in the appendix, optimizing for highest possible confidence results in adversarial noise that is clearly visible to the human eye. For $\kappa = 0.01$ and $\kappa = 1$ on the other hand, the applied noise is a lot harder to perceive by humans (See Fig. 23 and Fig. 26). We make a second important observation: For most models, the predictive confidence is similar to the ResNet. However, $\beta = 1$ and $\beta = 2$ are 100% confident in their (wrong) prediction, even for low values of κ . During the attack, this occurs while the fooling part of the loss is already satisfied and has no effect. The phenomenon is purely due to the attack reducing the amplitude of the perturbation. Evidently, by reducing the attack amplitude, the image moves into an even more confident region of latent space. So in the sense of predictive uncertainty on adversarial examples, GCs actually seem to be much less robust than DCs.

Adversarial Attack Detection We now frame the adversarial attack detection as an outlier detection problem and perform the OoD test described in Sec. 3.3.

The easiest case to detect is clearly $\kappa = \infty$, where most GC models achieve a perfect ROC-AUC of 100%. For $\kappa = 1$ and $\kappa = 0.01$, the situation is more challenging. With respect to beta, we find a bi-modal shape of the detection score: $\beta = 1$ performs best, with an ROC-AUC of $> 90\%$. $\beta = 32$ also perform fairly well, with a large decrease in between these two values. For datasets such as MNIST and SVHN, results are inconsistent and reported in different ways [43, 34, 18], but roughly speaking, the detection capability for $\beta = 1$ seems slightly worse or similar for ImageNet in comparison. Again, β could be reduced further, and we would expect an even better detection score.

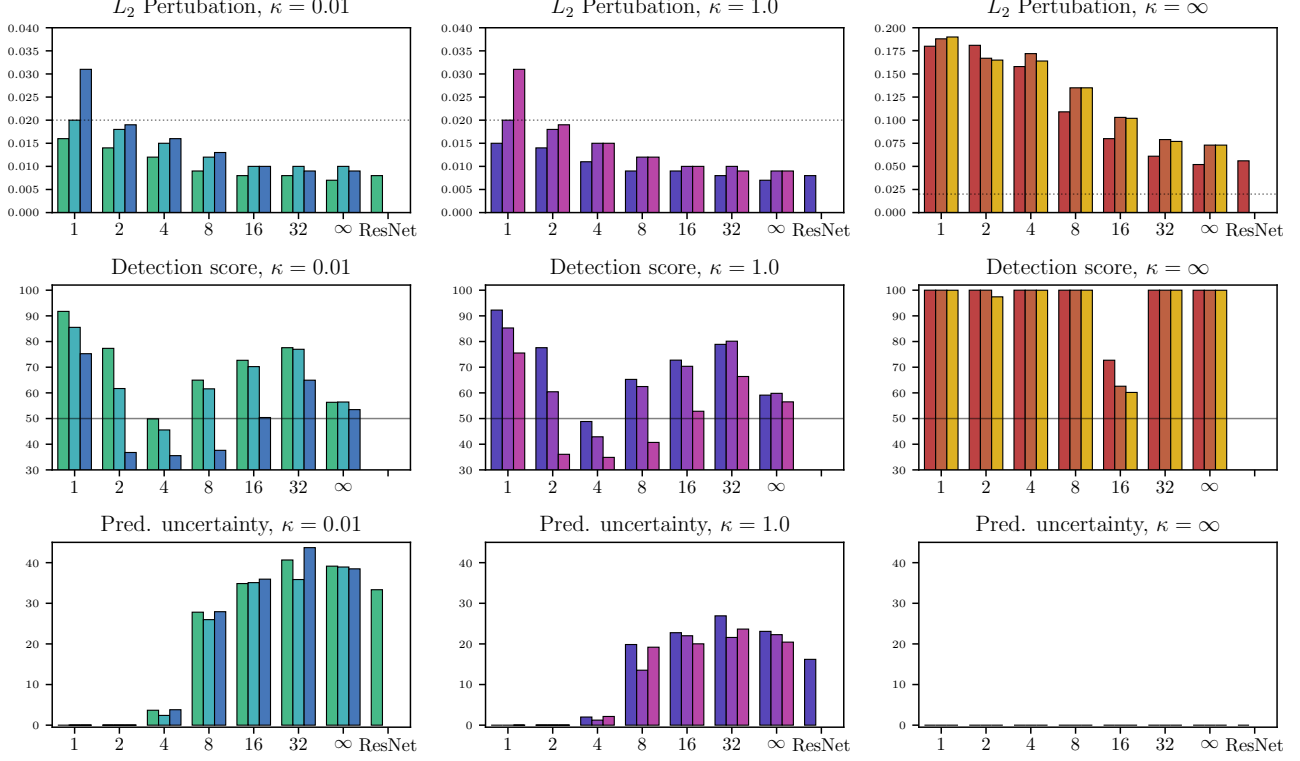


Figure 13: Behaviour of GCs under adversarial attacks. The three rows of plots give the mean perturbation, detection score, and uncertainty of the wrong prediction (1 – confidence). The three columns of plots correspond to adversarial attacks with $\kappa = 0.01$ (targeted prediction with any confidence is enough), $\kappa = 1$ (targeted prediction should have high confidence), and $\kappa = \infty$ (targeted prediction should be as confident as possible). The three bars for each β correspond to: standard adversarial attack ($d = 0$), as well as $d = 66$ and $d = 1000$, i.e. the detection mechanism is fooled at the same time as the prediction. The dotted line in the top row roughly indicates the level at which attacks are clearly visible by eye. Note that this is subjective and only a rough indication. The line in the second row indicates random performance, i.e. the OoD detection does nothing useful.

Attacking the Attack Detection Mechanism As illustrated previously in [7], any such defense- or detection mechanism can itself become target of a modified attack, fooling the classification and the detection at the same time. In line with this work, we construct a modified attack loss to achieve this. We denote it as $\mathcal{L}_{CWD}(w, x)$ (D for detection) in Eq. 25. In the added term, $\text{median}(\log(q_\theta(x_{\text{train}})))$ stands for the median estimated probability density (PD) of the training set and $\log(q_\theta(x_{\text{att}}))$ for the estimated PD of the perturbed image. Intuitively, we are now forcing x_{att} to move to the center of the distribution of PD values of the training data. If it reaches the median exactly, the ROC-AUC detection score will be 0%. In addition to $d = 0$ in Fig. 13 and Tables 7, 8, 9, we report results for a moderate ($d = 66$) and a very strong detection attack ($d = 1000$).

$$\mathcal{L}_{CWD}(w, x) = \mathcal{L}_{CW}(w, x) + d \left(\text{median}_{x' \sim X_{\text{train}}} (\log q_\theta(x')) - \log q_\theta(x_{\text{att}}(w)) \right)^2 \quad (25)$$

We make three observations: the adversarial noise is increased, when putting a higher focus on fooling the attack detection mechanism. This can also be clearly seen in Fig. 14 and in the quantitative comparison in Fig. 13, first row. Second, in the second row of Fig. 13, we observe the attack detection capabilities generally to decrease. For the good detection models such as $\beta = 1$, the score stays reasonably high, while the weaker models have a detection score significantly worse than random. Lastly, the predictive uncertainty is not affected by the detection attack at all (Fig. 13, third row).

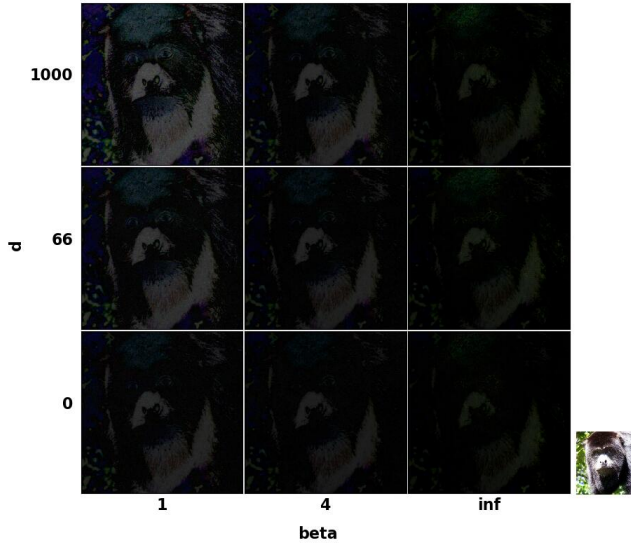


Figure 14: Qualitative results demonstrating the influence of d (controlling the strength put on fooling the attack detection mechanism) and β on adversarial attack robustness for κ fixed to 1. The more weight is put on fooling the attack detection mechanism (higher values for d), the more noise must be added to the input image by the adversarial attack. In order to fool the generally stronger detection mechanism of classifiers with higher generative modeling capabilities, the noise must be even higher.

Inspecting the attacked images also provides some clues as to how the attack fools the detection mechanism: They show uniformly decreased contrast. As shown in [35], such low-contrast images have unnaturally high estimated likelihoods. In our case, this seems to compensate for the lower estimated likelihood caused by the noise-like adversarial perturbations, to make the image appear ‘typical’ overall.

5. Conclusion

In this work, we have addressed the issue of trustworthiness in deep learning, in relation to generative classifiers (GCs). While many properties linked with trustworthiness are often ascribed to GCs, such as increased robustness and explainability, we feel it has so far not been shown clearly enough that these properties actually apply for tasks that are representative of real-world applications. In this regard, we have shown the methods used to train GCs on the ImageNet dataset, as well as the advantages and the limitation of using them compared to a standard discriminative classifier, the ResNet. Of course, the naive application of GCs does not solve all problems related to trustworthiness automatically. However, there are some significant improvements over standard DCs, especially in terms of explain-

ability and native out-of-distribution detection capabilities. From this, we conclude that GCs are a promising basis for trustworthy computer vision models, if further modifications and algorithms are developed, as have been for DCs in the past. We contribute the checkpoints for several GCs trained on ImageNet to the community in the hope that they will serve as a starting point for solving even more complex computer vision problems through GCs, and will help in designing more trustworthy classification models in the future.

6. Acknowledgements

RM received funding from the Robert Bosch PhD scholarship. LA received funding by the Federal Ministry of Education and Research of Germany project High Performance Deep Learning Framework (No 01IH17002). UK and CR received financial support from the European Research Council (ERC) under the European Unions Horizon 2020 research and innovation program (grant agreement No 647769). We thank the Center for Information Services and High Performance Computing (ZIH) at Dresden University of Technology for generous allocations of computation time.

Furthermore we thank our colleagues (alphabetically), Tim Adler, Felix Draxler, Jakob Kruse, Titus Leistner, Jens Mueller, and Peter Sorrenson for their help, support and fruitful discussions.

References

- [1] Lynton Ardizzone, Jakob Kruse, Carsten Rother, and Ullrich Köthe. Analyzing inverse problems with invertible neural networks. In *Intl. Conf. on Learning Representations*, 2019. 5, 19
- [2] Lynton Ardizzone, Carsten Lüth, Jakob Kruse, Carsten Rother, and Ullrich Köthe. Guided image generation with conditional invertible neural networks. *arXiv preprint arXiv:1907.02392*, 2019. 4, 5, 20
- [3] Lynton Ardizzone, Radek Mackowiak, Carsten Rother, and Ullrich Köthe. Training normalizing flows with the information bottleneck for competitive generative classification. *arXiv preprint arXiv:2001.06448*, 2020. 2, 3, 4, 8, 10
- [4] Jens Behrmann, David Duvenaud, and Jörn-Henrik Jacobsen. Invertible residual networks. *arXiv:1811.00995*, 2018. 3, 19
- [5] Christopher M. Bishop and Julia Lasserre. Generative or discriminative? getting the best of both worlds. *Bayesian statistics*, 8(3):3–24, 2007. 3
- [6] Guillaume Bouchard and Bill Triggs. The tradeoff between generative and discriminative classifiers. In *16th IASC International Symposium on Computational Statistics (COMPSTAT’04)*, pages 721–728, 2004. 3
- [7] Nicholas Carlini and David Wagner. Adversarial examples are not easily detected: Bypassing ten detection methods. In

- Proceedings of the 10th ACM Workshop on Artificial Intelligence and Security*, pages 3–14, 2017. 15
- [8] Nicholas Carlini and David A. Wagner. Towards evaluating the robustness of neural networks. In *2017 IEEE Symposium on Security and Privacy, SP 2017, San Jose, CA, USA, May 22-26, 2017*, pages 39–57. IEEE Computer Society, 2017. 12, 13
- [9] Jiefeng Chen, Yixuan Li, Xi Wu, Yingyu Liang, and Somesh Jha. Robust out-of-distribution detection in neural networks. *CoRR*, abs/2003.09711, 2020. 12
- [10] Hyunsun Choi, Eric Jang, and Alexander A Alemi. Waic, but why? generative ensembles for robust anomaly detection. *arXiv preprint arXiv:1810.01392*, 2018. 3
- [11] LI Chongxuan, Taufik Xu, Jun Zhu, and Bo Zhang. Triple generative adversarial nets. In *Advances in neural information processing systems*, pages 4088–4098, 2017. 3
- [12] Terrance DeVries and Graham W. Taylor. Learning confidence for out-of-distribution detection in neural networks. *CoRR*, abs/1802.04865, 2018. 2
- [13] Laurent Dinh, David Krueger, and Yoshua Bengio. NICE: Non-linear independent components estimation. *arXiv:1410.8516*, 2014. 3, 19
- [14] Laurent Dinh, Jascha Sohl-Dickstein, and Samy Bengio. Density estimation using Real NVP. *arXiv:1605.08803*, 2016. 3, 5, 19, 20
- [15] Vincent Dumoulin, Jonathon Shlens, and Manjunath Kudlur. A learned representation for artistic style. In *Intl. Conf. on Learning Representations*, 2017. 3
- [16] Ethan Fetaya, Jörn-Henrik Jacobsen, Will Grathwohl, and Richard S. Zemel. Understanding the limitations of conditional generative models. In *8th International Conference on Learning Representations, ICLR 2020, Addis Ababa, Ethiopia, April 26-30, 2020*. OpenReview.net, 2020. 2
- [17] Ethan Fetaya, Jörn-Henrik Jacobsen, and Richard S. Zemel. Conditional generative models are not robust. *CoRR*, abs/1906.01171, 2019. 2, 3, 4
- [18] Partha Ghosh, Arpan Losalka, and Michael J. Black. Resisting adversarial attacks using gaussian mixture variational autoencoders. In *The Thirty-Third AAAI Conference on Artificial Intelligence, AAAI 2019, The Thirty-First Innovative Applications of Artificial Intelligence Conference, IAAI 2019, The Ninth AAAI Symposium on Educational Advances in Artificial Intelligence, EAAI 2019, Honolulu, Hawaii, USA, January 27 - February 1, 2019*, pages 541–548. AAAI Press, 2019. 3, 14
- [19] Leilani H Gilpin, David Bau, Ben Z Yuan, Ayesha Bajwa, Michael Specter, and Lalana Kagal. Explaining explanations: An overview of interpretability of machine learning. In *2018 IEEE 5th International Conference on data science and advanced analytics (DSAA)*, pages 80–89. IEEE, 2018. 2
- [20] Will Grathwohl, Ricky TQ Chen, Jesse Betterncourt, Ilya Sutskever, and David Duvenaud. Ffjord: Free-form continuous dynamics for scalable reversible generative models. *arXiv preprint arXiv:1810.01367*, 2018. 3
- [21] Will Grathwohl, Kuan-Chieh Wang, Jörn-Henrik Jacobsen, David Duvenaud, Mohammad Norouzi, and Kevin Swersky. Your classifier is secretly an energy based model and you should treat it like one. *arXiv preprint arXiv:1912.03263*, 2019. 3
- [22] Kaiming He, Xiangyu Zhang, Shaoqing Ren, and Jian Sun. Deep residual learning for image recognition. In *Proceedings of the IEEE conference on computer vision and pattern recognition*, pages 770–778, 2016. 2, 6, 19, 21
- [23] Dan Hendrycks and Thomas G. Dietterich. Benchmarking neural network robustness to common corruptions and perturbations. In *7th International Conference on Learning Representations, ICLR 2019, New Orleans, LA, USA, May 6-9, 2019*, 2019. 2
- [24] Dan Hendrycks and Thomas G. Dietterich. Benchmarking neural network robustness to common corruptions and perturbations. In *7th International Conference on Learning Representations, ICLR 2019, New Orleans, LA, USA, May 6-9, 2019*. OpenReview.net, 2019. 12
- [25] Yen-Chang Hsu, Yilin Shen, Hongxia Jin, and Zsolt Kira. Generalized ODIN: detecting out-of-distribution image without learning from out-of-distribution data. *CoRR*, abs/2002.11297, 2020. 12
- [26] Xiaowei Huang, Daniel Kroening, Wenjie Ruan, James Sharp, Youcheng Sun, Emese Thamo, Min Wu, and Xinping Yi. A survey of safety and trustworthiness of deep neural networks. *arXiv preprint arXiv:1812.08342*, 2018. 2
- [27] Pavel Izmailov, Polina Kirichenko, Marc Finzi, and Andrew Gordon Wilson. Semi-supervised learning with normalizing flows. *arXiv preprint arXiv:1912.13025*, 2019. 4
- [28] Jörn-Henrik Jacobsen, Jens Behrmann, Richard Zemel, and Matthias Bethge. Excessive invariance causes adversarial vulnerability. *arXiv preprint arXiv:1811.00401*, 2018. 5, 6, 20
- [29] Jörn-Henrik Jacobsen, Arnold W.M. Smeulders, and Edouard Oyallon. i-RevNet: deep invertible networks. In *International Conference on Learning Representations*, 2018. 3, 7, 20
- [30] Diederik P Kingma and Prafulla Dhariwal. Glow: Generative flow with invertible 1x1 convolutions. *arXiv:1807.03039*, 2018. 5, 19
- [31] Durk P Kingma, Shakir Mohamed, Danilo Jimenez Rezende, and Max Welling. Semi-supervised learning with deep generative models. In *Advances in neural information processing systems*, pages 3581–3589, 2014. 3
- [32] Kimin Lee, Kibok Lee, Honglak Lee, and Jinwoo Shin. A simple unified framework for detecting out-of-distribution samples and adversarial attacks. In Samy Bengio, Hanna M. Wallach, Hugo Larochelle, Kristen Grauman, Nicolò Cesa-Bianchi, and Roman Garnett, editors, *Advances in Neural Information Processing Systems 31: Annual Conference on Neural Information Processing Systems 2018, NeurIPS 2018, 3-8 December 2018, Montréal, Canada*, pages 7167–7177, 2018. 12
- [33] Kimin Lee, Sukmin Yun, Kibok Lee, Honglak Lee, Bo Li, and Jinwoo Shin. Robust inference via generative classifiers for handling noisy labels. *arXiv preprint arXiv:1901.11300*, 2019. 3

- [34] Yingzhen Li, John Bradshaw, and Yash Sharma. Are generative classifiers more robust to adversarial attacks? In Kamalika Chaudhuri and Ruslan Salakhutdinov, editors, *Proceedings of the 36th International Conference on Machine Learning, ICML 2019, 9-15 June 2019, Long Beach, California, USA*, volume 97 of *Proceedings of Machine Learning Research*, pages 3804–3814. PMLR, 2019. 2, 3, 12, 14
- [35] Eric T. Nalisnick, Akihiro Matsukawa, Yee Whye Teh, Dilan Görür, and Balaji Lakshminarayanan. Do deep generative models know what they don’t know? In *7th International Conference on Learning Representations, ICLR 2019, New Orleans, LA, USA, May 6-9, 2019*, 2019. 2, 3, 5, 16
- [36] Eric T. Nalisnick, Akihiro Matsukawa, Yee Whye Teh, Dilan Görür, and Balaji Lakshminarayanan. Hybrid models with deep and invertible features. In *Proceedings of the 36th International Conference on Machine Learning, ICML 2019, 9-15 June 2019, Long Beach, California, USA*, pages 4723–4732, 2019. 3
- [37] Eric T. Nalisnick, Akihiro Matsukawa, Yee Whye Teh, and Balaji Lakshminarayanan. Detecting out-of-distribution inputs to deep generative models using a test for typicality. *CoRR*, abs/1906.02994, 2019. 3, 5
- [38] Andrew Y. Ng and Michael I. Jordan. On discriminative vs. generative classifiers: A comparison of logistic regression and naive bayes. In *Advances in Neural Information Processing Systems 14 [Neural Information Processing Systems: Natural and Synthetic, NIPS 2001, December 3-8, 2001, Vancouver, British Columbia, Canada]*, pages 841–848, 2001. 3
- [39] Aaron van den Oord, Nal Kalchbrenner, and Koray Kavukcuoglu. Pixel recurrent neural networks. *arXiv preprint arXiv:1601.06759*, 2016. 7
- [40] Rajat Raina, Yirong Shen, Andrew McCallum, and Andrew Y Ng. Classification with hybrid generative/discriminative models. In *Advances in neural information processing systems*, pages 545–552, 2004. 3
- [41] Christian Raymond and Giuseppe Riccardi. Generative and discriminative algorithms for spoken language understanding. In *Eighth Annual Conference of the International Speech Communication Association*, 2007. 2, 3
- [42] Olga Russakovsky, Jia Deng, Hao Su, Jonathan Krause, Sanjeev Satheesh, Sean Ma, Zhiheng Huang, Andrej Karpathy, Aditya Khosla, Michael Bernstein, Alexander C. Berg, and Li Fei-Fei. ImageNet large scale visual recognition challenge. *International Journal of Computer Vision (IJCV)*, 115(3):211–252, 2015. 7
- [43] Lukas Schott, Jonas Rauber, Matthias Bethge, and Wieland Brendel. Towards the first adversarially robust neural network model on MNIST. In *7th International Conference on Learning Representations, ICLR 2019, New Orleans, LA, USA, May 6-9, 2019*. OpenReview.net, 2019. 3, 12, 14
- [44] Ramprasaath R Selvaraju, Michael Cogswell, Abhishek Das, Ramakrishna Vedantam, Devi Parikh, and Dhruv Batra. Grad-cam: Visual explanations from deep networks via gradient-based localization. In *Proceedings of the IEEE international conference on computer vision*, pages 618–626, 2017. 10
- [45] Jasper Snoek, Yaniv Ovadia, Emily Fertig, Balaji Lakshminarayanan, Sebastian Nowozin, D Sculley, Joshua Dillon, Jie Ren, and Zachary Nado. Can you trust your model’s uncertainty? evaluating predictive uncertainty under dataset shift. In *Advances in Neural Information Processing Systems*, pages 13969–13980, 2019. 12
- [46] Christian Szegedy, Vincent Vanhoucke, Sergey Ioffe, Jon Shlens, and Zbigniew Wojna. Rethinking the inception architecture for computer vision. In *Proceedings of the IEEE conference on computer vision and pattern recognition*, pages 2818–2826, 2016. 21
- [47] Christian Szegedy, Wojciech Zaremba, Ilya Sutskever, Joan Bruna, Dumitru Erhan, Ian J. Goodfellow, and Rob Fergus. Intriguing properties of neural networks. In *2nd International Conference on Learning Representations, ICLR 2014, Banff, AB, Canada, April 14-16, 2014, Conference Track Proceedings*, 2014. 2
- [48] Esteban G Tabak and Cristina V Turner. A family of non-parametric density estimation algorithms. *Communications on Pure and Applied Mathematics*, 66(2):145–164, 2013. 4
- [49] Lucas Theis, Aäron van den Oord, and Matthias Bethge. A note on the evaluation of generative models. *arXiv preprint arXiv:1511.01844*, 2015. 7
- [50] Naftali Tishby, Fernando C. N. Pereira, and William Bialek. The information bottleneck method. *CoRR*, physics/0004057, 2000. 4
- [51] Jakub M Tomczak and Max Welling. Improving variational auto-encoders using household flow. *arXiv preprint arXiv:1611.09630*, 2016. 19
- [52] Ilkay Ulusoy and Christopher M. Bishop. Comparison of generative and discriminative techniques for object detection and classification. In *Toward Category-Level Object Recognition*, pages 173–195, 2006. 3
- [53] Christina Winkler, Daniel Worrall, Emiel Hoogeboom, and Max Welling. Learning likelihoods with conditional normalizing flows. *arXiv preprint arXiv:1912.00042*, 2019. 4
- [54] Han Xu, Yao Ma, Haochen Liu, Debayan Deb, Hui Liu, Jiliang Tang, and Anil Jain. Adversarial attacks and defenses in images, graphs and text: A review. *arXiv preprint arXiv:1909.08072*, 2019. 12
- [55] Jing-Hao Xue and D. M. Titterton. On the generative-discriminative tradeoff approach: Interpretation, asymptotic efficiency and classification performance. *Computational Statistics & Data Analysis*, 54(2):438–451, 2010. 3
- [56] Bolei Zhou, Aditya Khosla, Agata Lapedriza, Aude Oliva, and Antonio Torralba. Learning deep features for discriminative localization. In *Proceedings of the IEEE conference on computer vision and pattern recognition*, pages 2921–2929, 2016. 10

– Appendix –

A. Network Architecture Details

In the following, we outline the design choices and training procedure used for training the INN model as a GC on the ImageNet dataset. It has been noted in the past that there are strong parallels between ResNet residual blocks [22] and INN affine coupling blocks [14], described further below. In fact, under some additional constraints, standard ResNet residual blocks can also be numerically inverted [4]. Therefore, a standard ResNet is not only the most fitting comparison to our GC, but also informs many of our design choices. The argument is, that ResNets contain many carefully tested design choices, leading to their excellent discriminative performance. Adopting these choices where possible saves us from performing an infeasible number of ablations and comparisons ourselves, and still achieve relatively good performance empirically.

Affine coupling operation. As a basic building block of our network, we use the affine coupling block shown in Fig. 15. Such blocks were first introduced in [14], and are exactly and cheaply invertible, as well as having a tractable Jacobian determinant. The incoming features are first split in two halves, say u_1 and u_2 , along the channel dimension. The first half u_1 is not changed, and passed straight through. A subnetwork, similar to the residual subnetwork of a ResNet then predicts affine coefficients s, t from u_1 , which are used to perform an affine transformation on the other half of the features u_2 . This gives us outputs v_1, v_2 :

$$v_2 = s(u_1) \odot u_2 + t(u_1) \quad \text{and} \quad v_1 = u_1 \quad (26)$$

To invert this operation given only v_1, v_2 , note that $u_1 = v_1$ is trivially available, so the same coefficients s, t can be re-computed for the inverse. With these, the affine transformation itself can be analytically inverted, to get back $u_2 = (v_2 - t(v_1)) \oslash s(v_1)$. To guarantee invertibility, we restrict $s(\cdot) > 0$. In theory, $s(\cdot) \neq 0$ suffices, but this complicates the situation and does not improve expressive power: mirroring an output dimension is irrelevant for the network and the loss. We ensure $s(\cdot) > 0$ by using $\exp(\alpha \tanh(\cdot))$ activation on the s -outputs of the subnetwork, as previously in [14], where α is a fixed hyperparameter. In principle, \exp alone would be enough, but this leads to instabilities during training, as it can become infinitely large. Importantly to note, the subnetwork itself never has to be inverted, and is always computed forward. Therefore, it can contain the usual operations such as convolutions or batch normalization.

To compare, in a standard ResNet block, a copy operation is used instead of the split, and a simple addition is

performed in place of the affine transformation. Apart from this, the structure is very similar.

Complete coupling blocks. The expressive power of the affine coupling above is insufficient: half the data is not touched at all, and the remaining variables can only be scaled up/down by a factor of at most $\exp(\pm\alpha)$. We add two more invertible operations to solve these problems: We first perform a global channel-wise affine transformation to all variables with scaling s_{global} and bias t_{global} . This technique was already proposed in [14] and refined in [30] as ‘ActNorm’. Note that in feed-forward networks, this is also often done as part of the batch normalization layers. Again, s_{global} must be positive, and we achieve the best results choosing $s_{\text{global}} = s_0 \text{softplus}(\gamma) = s_0 \log(1 + e^\gamma)$. Here, γ and t_{global} are learned directly as free parameters, and s_0 is a scalar hyperparameter which we fix to 0.1, while γ is initialized to 10.

Secondly, we want to use a different split in the next block, and therefore have to apply some invertible operation that mixes the channels. So far, there is no ‘default’ approach to this in the INN literature. Various methods exist, such as simply swapping the two halves [13], learned householder reflections [51], fixed permutations [1], and learning unconstrained mixing matrices [30], among others. While it is desirable to use a learned mixing operations, we do not find any benefits in practice. The method used for [30] has no guaranteed invertibility, and the training can simply crash when the matrix becomes singular. The householder matrices from [51] quickly become computationally expensive with many reflections, and in our case bring no empirical benefit over fixed (not learned) mixing. Instead, we use a random orthogonal matrix from the $O(N)$ Haar distribution after each coupling block, that stays fixed during training. This encourages more mixing than a simple hard permutation, and empirically gives the best results with our architecture.

With an orthogonal mixing matrix, the overall log-Jacobian-determinant of one coupling block can be shown to be

$$\log |\det(J)| = \sum \log s(u_1) + \sum \log s_{\text{global}}. \quad (27)$$

Due to the chain rule, and product decomposition of the determinant, the sum of the log-Jac-det of each coupling block will give the log-Jac-det of the entire network. An illustration of a coupling block is given in Fig. 15, left.

Subnetworks. We adopt the ResNet design choices for building the affine subnetworks, with one modification: we

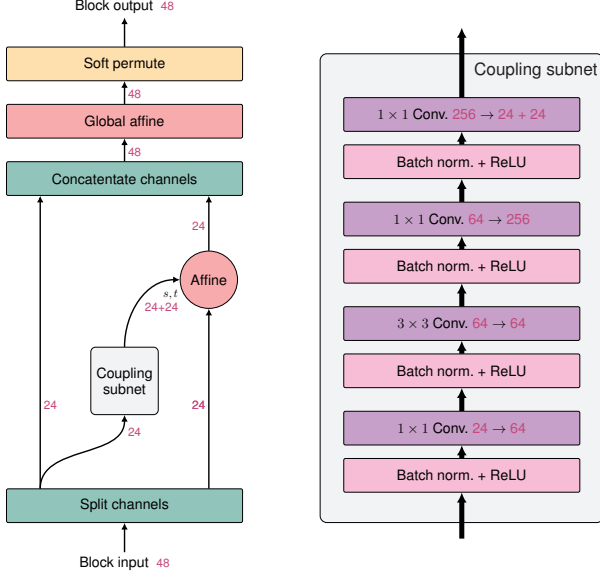


Figure 15: Illustration of the coupling blocks used, as well as the structure of the subnetworks used to predict the affine components. The purple numbers indicate the number of feature channels, given as an example for the first resolution level (see Table 1, *Conv_2_x*).

add an additional 1×1 projection layer as the final output. This is motivated by the fact that the INN has less feature maps than the ResNet for all but the last resolution level. Therefore, the expressive power would be limited by only having this few output channels for the final convolution. The subnetwork design is shown in Fig. 15, right.

Downsampling blocks. In the past, various invertible downsampling operations have been used, e.g. [14, 29, 2]. Notably, none of these have a learnable component, such as strided convolutions. Instead, we introduce a *downsampling coupling block*, as a natural extension of the downsampling residual blocks present at the end of each ResNet section. Shown in more detail in Fig. 16, we use two of the invertible re-ordering and re-shaping operations from [29], but nested within a single coupling block. This way, the subnetwork can make use of a strided 3×3 convolution as a learned component to the downsampling. Note that we did not perform rigorous ablations of this introduction, and chose it mainly for better conformity to standard ResNets.

Network layout. The overall network layout is the same as for the standard ResNet-50, which offers a good trade-off between performance and model complexity. The input images are immediately downsampled twice, once using a downsampling coupling block with a 7×7 convolution, then with a Haar wavelet transform as in [2]. The ResNet ana-

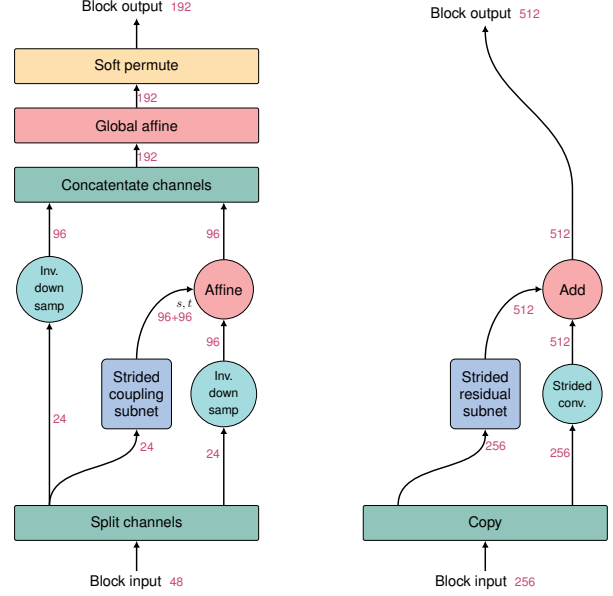


Figure 16: Illustration of our downsampling coupling blocks (left), compared to the standard ResNet downsampling blocks (right). The invertible downsampling operation (blue circles) reorders inputs in a checkerboard pattern as in [29].

Layer	Blocks	Im. size	Channels		R.F.	
			INN	ResNet	INN	ResNet
Input		224	3	3		
Entry flow	1	112	12	64	8	6
Pool (Haar/max)		56	48	64	10	10
Conv_2_x	3	56	48	256	34	34
Conv_3_x	4	28	192	512	106	90
Conv_4_x	6	14	768	1024	314	266
Conv_5_x	3	7	3072	2048	538	426
Pool (DCT/avg.)		1	150 528	2048	∞	∞

Table 6: For each of the resolution levels in the INN and ResNet-50, the number of coupling/residual blocks and spatial size is given, along with the number of feature channels and the maximum possible receptive field (R.F.).

logue is the so-called *entry flow*, which also uses a strided 7×7 convolution and a max-pooling operation. A series of coupling blocks follow this, with downsampling blocks distributed throughout, chosen in the same way as for the ResNet-50, detailed in Tab. 1. The output of the INN consists of 3072 two dimensional feature maps at a resolution of 7×7 (compared to 2048 feature maps for the ResNet).

In the ResNet, the output feature maps are passed through a global mean pooling operation. As explained in [28], a discrete cosine transform (DCT) presents the best invertible alternative to this: From our 3072 feature maps, the DCT also produces mean pooled outputs, along with 48 other outputs per feature map, that encode the remaining in-

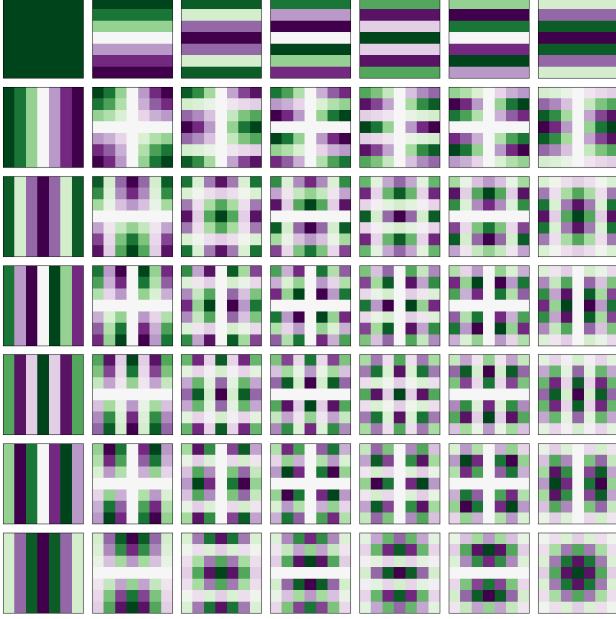


Figure 17: Each 7×7 feature map is transformed to 49 orthogonal output features, using the DCT coefficients shown above. Green > 0 , Purple < 0 , white $= 0$. The top left most output feature is equal to the mean pooling operation.

formation. The DCT coefficients are visualized in Fig. 17. As a final step, the ResNet performs a linear projection to the 1000 logits. The analogous operation for the INN is taking the distance of the output z to each of the 1000 cluster centers.

Low-rank μ_y . If each entry of μ_y is learned independently, the total number of parameters for D -dimensional latent space and M classes will be $DM \approx 150$ Mil for ImageNet. This is completely impractical, as μ_y alone would make up the majority of network parameters, which will only lead to overfitting. We solve this by dividing up μ_y into two parts, corresponding to the mean-pooled and the higher-order DCT variables: $\mu_y = [\mu_{\text{mean},y}, \mu_{\text{rest},y}]$. We freely learn all approx. 3 Mil parameters of $\mu_{\text{mean},y}$, and choose a low-rank representation for the remaining $\mu_{\text{rest},y}$, using K prototype vectors μ_k :

$$\mu_{\text{rest},y} = \sum_{k=1}^K \alpha_{yk} \mu_k \quad (28)$$

Both μ_k and α_{yk} are learned. This reduces the number of parameters to $D_{\text{mean}}M + K(D_{\text{rest}} + M)$. Choosing $K = 128$ empirically gives the best validation performance, and results in approx. 19 Mil parameters, almost a factor of 10 less than the full DM . However, it is important to note that this is still much more than the fully connected layer

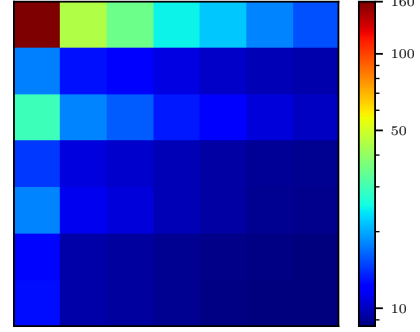


Figure 18: For the 49 DCT components images shown in Fig. 17, the mean spread of the corresponding entries of μ_y across classes is shown. Intuitively, this is how much each DCT component contributes to classification. A value of 0 means that these dimensions do not affect the classification at all. The mean pooled component has by far the largest influence, and the contribution of the high order components (bottom right) is negligible. Due to the random horizontal flip augmentation, the horizontally anti-symmetric components hardly contribute (alternating rows).

of a standard ResNet, with approx. 2 Mil parameters. This indicates it might be possible to find an even more efficient representation of μ_y without sacrificing performance. The influence of each component of the low-rank μ_y is shown in Fig. 18. While $\mu_{\text{mean},y}$ contributes by far the most, training without $\mu_{\text{rest},y}$ entirely (setting it to zero), degrades the validation top-1 prediction performance by several percentage points.

Data augmentation and training. As data augmentation, we perform the usual random crops and horizontal flips, with two additions: Firstly, as is standard practice with normalizing flows specifically, we add uniform noise with amplitude $1/255$ to the images, to remove the quantization. This is necessary when training with the Jacobian, as the quantization otherwise leads to problems. Secondly, we use label smoothing [46] with $\alpha = 0.05$. This is necessary to prevent the mixture centroids from drifting further and further apart: training with perfectly hard labels makes the implicit assumption that all class components are infinitely separated.

The training scheme is the same as for the standard ResNet [22]: we use the SGD optimizer with a momentum of 0.9 and the weight decay set to 0.0001. We set the initial learning rate slightly lower to 0.07 compared to 0.1 for the original ResNet. We also perform two subsequent cooling steps whenever the loss plateaus, decreasing the learning rate by a factor of 10 each time. The batch size is 64 per

GPU, training on 6 GPUs.

B. Expected Predictive Uncertainty

For the pairwise predictive uncertainty, we only consider two classes, $y \in \{1, 2\}$. We denote the distance of the class centers as $\Delta\mu = \|\mu_1 - \mu_2\|$. We assume $y = 1$ is the top prediction. This is just for simplification, as 1 and 2 can be swapped in the derivation if $y = 2$ is the top prediction. The prediction confidence c for any latent vector z is then between 0.5 and 1.0, computed as

$$c(z) = \frac{p(z \mid y=1)}{p(z \mid y=1) + p(z \mid y=2)} \quad (29)$$

If the model has converged correctly, the latent distribution will be

$$p(Z) = \frac{1}{2}\mathcal{N}(\mu_1; 1) + \frac{1}{2}\mathcal{N}(\mu_2; 1) \quad (30)$$

This allows us to explicitly work out how the confidences will be distributed through the change-of-variables formula. Note that z can be expressed in cylindrical coordinates oriented along the line connecting μ_1 and μ_2 . All the radial parts integrate out, only the position along this line is relevant. After some substitutions and simplifications, we obtain

$$p(c) = \frac{1}{A} \underbrace{(c - c^2)^{-3/2} \exp\left(-\frac{1}{2\Delta\mu^2} \log^2\left(\frac{1}{c} - 1\right)\right)}_{:=\rho(c)} \quad (31)$$

A is the normalization constant and has no closed form:

$$A = \int_{1/2}^1 \rho(c) dc \quad (32)$$

And we simply call the unnormalized density $\rho(c)$. Finally, the expected confidence \bar{C} can be readily computed as

$$\bar{C} = \frac{\int c\rho(c)dc}{\int \rho(c)dc} \quad (33)$$

The expected *uncertainty* as opposed to the confidence is simply $1 - \bar{C}$. We confirm our analytic computation using a Monte Carlo simulation of the two-class case, and get perfect agreement.

C. Additional Figures and Tables

This section provides the following additional materials:

- Adversarial trajectories for the full 1000-class model: Fig. 22.
- Tables with the precise numbers used in Fig. 13: Tables 7, 8, 9.
- Resulting images for each setting used in Fig. 13: Figs. 23 - 31.
- PCA visualizations of the latent space: Fig. 19.
- Calibration curves for all models: Fig. 20.
- More examples of adversarial trajectories for the model with a 2D decision space: Fig. 21.

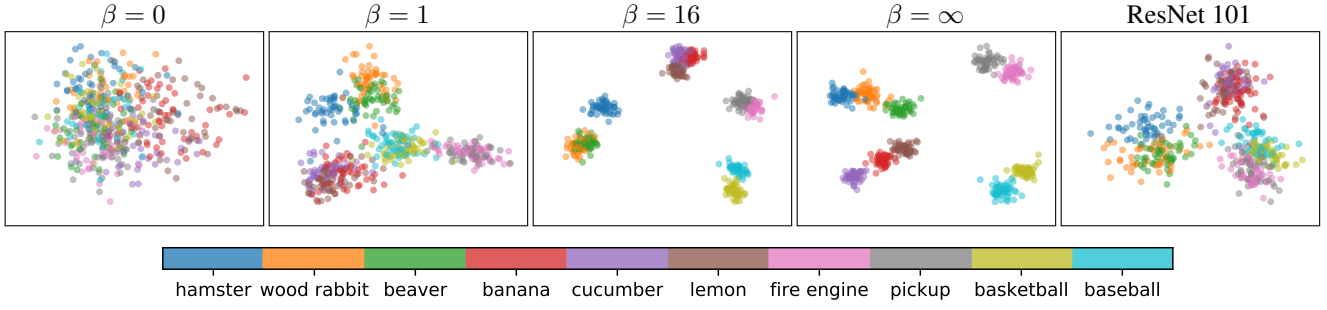


Figure 19: Layout of the learned GMM in latent space when the same architecture is trained with different values of β , with ResNet 50 shown for reference. As the ResNet does not explicitly model a GMM we performed an LDA projection of the 2nd-last layer onto two dimensions. Class separation improves as β increases, and no separation occurs at $\beta = 0$. Similar classes are grouped close to each other. Actual separation in the high-dimensional latent space is, of course, much better than in this two-dimensional projection.

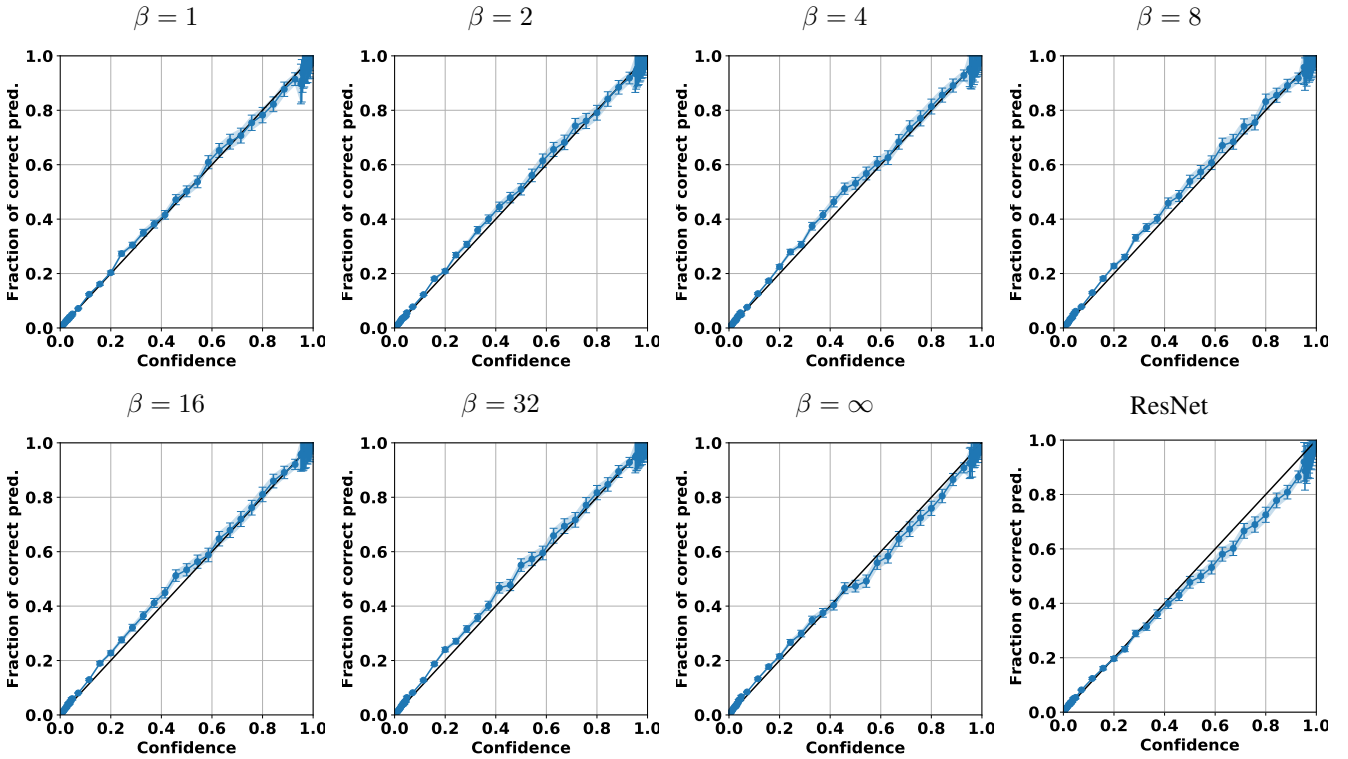


Figure 20: Calibration results for models trained with different values for β and the ResNet. All our GC's are better calibrated than the ResNet, which starts to get quite overconfident for expected probability values above 0.4. We also observe the model trained with $\beta = \text{infinity}$ to make overconfident predictions. As this model does not learn anything about $p(x)$ it can be considered a DC.

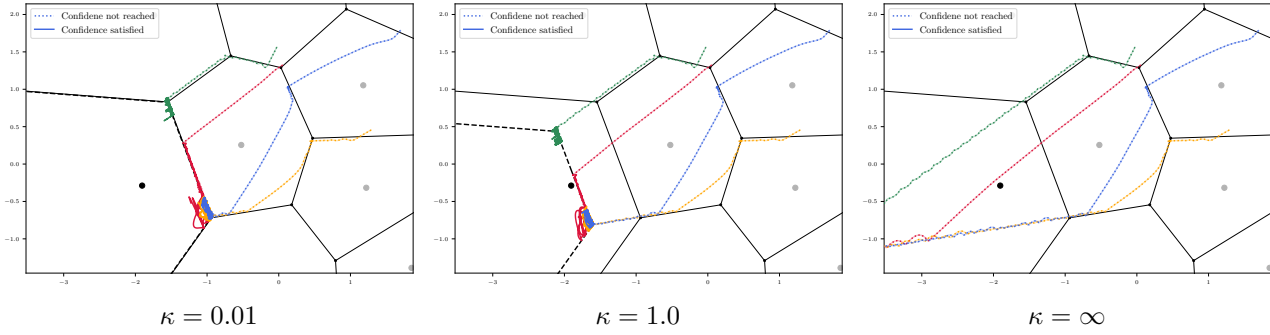


Figure 21: Additional examples for Fig. 11 with different settings for κ .

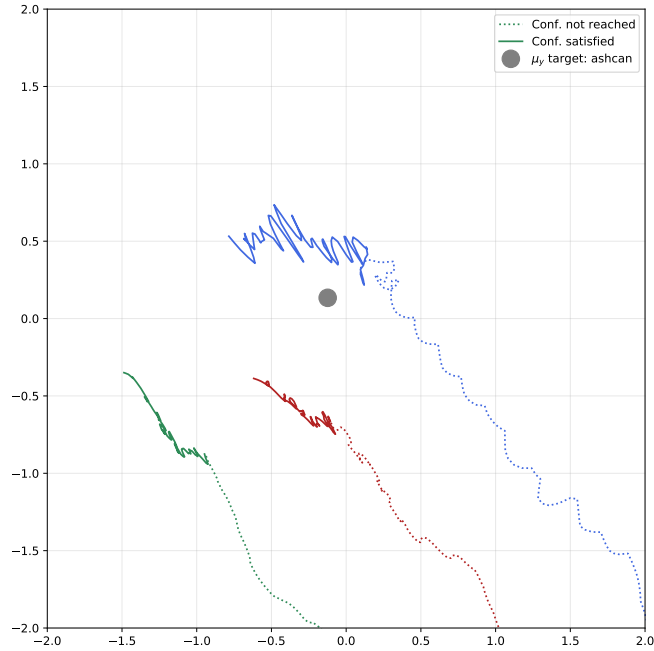


Figure 22: Visualization of the adversarial trajectories for the full model, $\kappa = 1$. The trajectory is projected to 2D by fitting a plane through the five classes that the trajectory passes closest to.

β	Confidence			Corruption			Success			OoD				X	Entropy			p(x) Val
	d=0	d=66	d=1000	d=0	d=66	d=1000	d=0	d=66	d=1000	1t-tt p(x)	p(x)				$X_{Corr.}$			
	d=0	d=66	d=1000	d=0	d=66	d=1000	d=0	d=66	d=1000	d=0	d=66	d=1000	d=1000		d=0	d=66	d=1000	
0	89.94	74.5	93.99	0.033	0.057	0.123	90	74	93	99.91	99.77	99.15	98.79	1.99	0	0	0	48.67
1	100	99.99	99.99	0.016	0.020	0.031	100	100	100	93.86	91.74	85.52	75.26	1.92	0	0	0	47.99
2	99.99	99.99	99.99	0.014	0.018	0.019	100	100	100	79.68	77.34	61.69	36.78	1.63	0	0	0	48.39
4	96.33	97.6	96.2	0.012	0.015	0.016	100	100	100	48.17	49.88	45.56	35.55	1.46	0.23	0.17	0.26	49.13
8	72.19	74.02	72.07	0.009	0.012	0.013	100	100	99	63.83	64.96	61.57	37.62	1.36	1.64	1.55	1.73	51.35
16	65.14	64.91	64.06	0.008	0.010	0.010	100	99	100	70.78	72.69	70.23	50.40	1.30	2.04	2.07	2.22	51.82
32	59.34	64.15	56.3	0.008	0.010	0.009	100	98	98	76.24	77.60	76.98	64.94	1.28	2.39	2.07	2.58	53.23
infinity	60.86	61.07	61.52	0.007	0.010	0.009	100	98	98	56.41	56.33	56.44	53.48	1.09	2.23	2.17	2.20	52.12
RN	66.66	-	-	0.008	-	-	100	-	-	-	-	-	-	1.02	1.84	-	-	-

Table 7: $\kappa = 0.01$

β	Confidence			Corruption			Success			OoD				X	Entropy $X_{Corr.}$			p(x) Val
	d=0	d=66	d=1000	d=0	d=66	d=1000	d=0	d=66	d=1000	1t-tt p(x)	p(x)				d=0	d=66	d=1000	
0	91.50	77.5	94.5	0.032	0.056	0.122	91	77	94	99.50	99.38	99.35	98.89	1.99	0	0	0	48.67
1	100	100	99.99	0.015	0.020	0.031	100	100	100	94.26	92.25	85.28	75.53	1.92	0	0	0	47.99
2	99.99	99.99	99.99	0.014	0.018	0.019	100	100	100	80.22	77.60	60.43	36.07	1.63	0	0	0	48.39
4	98.0	98.76	97.86	0.011	0.015	0.015	100	100	100	48.98	48.85	42.89	34.87	1.46	0.11	0.09	0.15	49.13
8	80.15	86.47	80.81	0.009	0.012	0.012	100	100	100	63.98	65.25	62.47	40.70	1.36	1.26	0.86	1.26	51.35
16	77.24	77.99	79.98	0.009	0.010	0.010	100	100	100	70.99	72.75	70.35	52.84	1.30	1.46	1.37	1.30	51.82
32	73.09	78.41	76.35	0.008	0.010	0.009	100	100	100	77.79	78.90	80.13	66.38	1.28	1.68	1.34	1.54	53.23
infinity	76.91	77.72	79.56	0.007	0.009	0.009	100	100	100	59.09	59.12	59.82	56.50	1.09	1.44	1.38	1.28	52.12
RN	83.8	-	-	0.08	-	-	100	-	-	-	-	-	-	1.00	1.15	-	-	-

Table 8: $\kappa = 1$

β	Confidence			Corruption			Success			OoD				X	Entropy			p(x) Val
	d=0	d=66	d=1000	d=0	d=66	d=1000	d=0	d=66	d=1000	1t-tt p(x)	p(x)				$X_{Corr.}$	d=66	d=1000	
										d=0	d=66	d=1000						
0	100	100	100	0.231	0.237	0.237	100	100	100	100	100	100	100	1.99	0	0	0	48.67
1	100	100	100	0.180	0.188	0.190	100	100	100	100	100	100	99.98	1.92	0	0	0	47.99
2	100	100	100	0.181	0.167	0.165	100	100	100	100	100	100	97.41	1.63	0	0	0	48.39
4	100	100	100	0.158	0.172	0.164	100	100	100	100	100	100	99.98	1.46	0	0	0	49.13
8	100	100	100	0.109	0.135	0.135	100	100	100	100	100	100	100	1.36	0	0	0	51.35
16	100	100	100	0.080	0.103	0.102	100	100	100	73.05	72.72	62.59	60.17	1.30	0	0	0	51.82
32	100	100	100	0.061	0.079	0.077	100	100	100	99.97	100	100	100	1.28	0	0	0	53.23
infinity	100	100	100	0.052	0.073	0.073	100	100	100	99.98	99.98	99.97	99.97	1.09	0	0	0	52.12
RN	100	-	-	0.056	-	-	100	-	-	-	-	-	-	1.04	0	-	-	-

Table 9: $\kappa = \infty$

Table 10: Table 7, 8 and 9 show the quantitative results of our adversarial attack experiments. Each table was obtained by performing the attack with a different value for $\kappa \in 0.01, 1, \text{inf}$. A high value for κ aims a more certain posterior for targeted classes. The cell background colors green, orange and red stand for different values for d to ease the comparison across models and tables for a human reader. The variable d quantifies the strength on fooling the intrinsic attack detection mechanism of our learned classifiers. Note, that the ResNet does not model the data likelihood and therefore has not this capability. We report the maximum class probability (Confidence), the pixel-wise l^2 -distance between the original and the adversarially perturbed image averaged over all pixels (Corruption), the success rate of the attack (Success), the one (1t-tt) and two-tailed ($p(x)$) typicality test OoD detection scores, as well as the posterior predictive uncertainty for the original (X) and the corrupted validation data $x_{corr.}$. Furthermore, we report the likelihood of the original validation data ($p(X)$ Val).

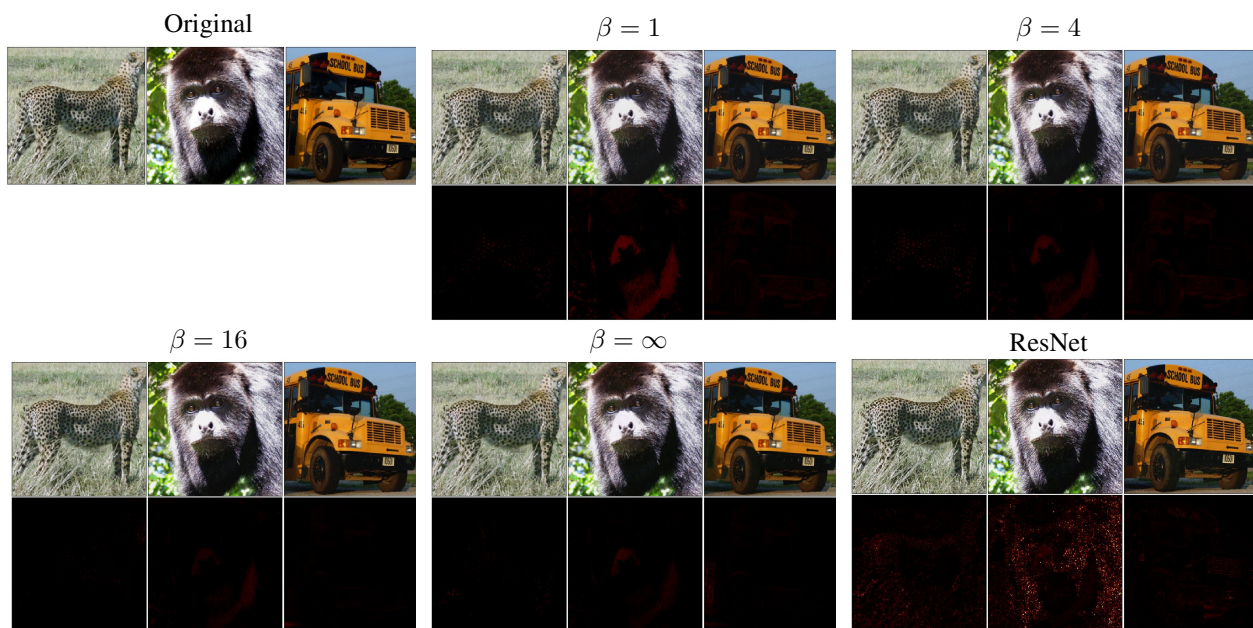


Figure 23: $\kappa = 0.01, d = 0$

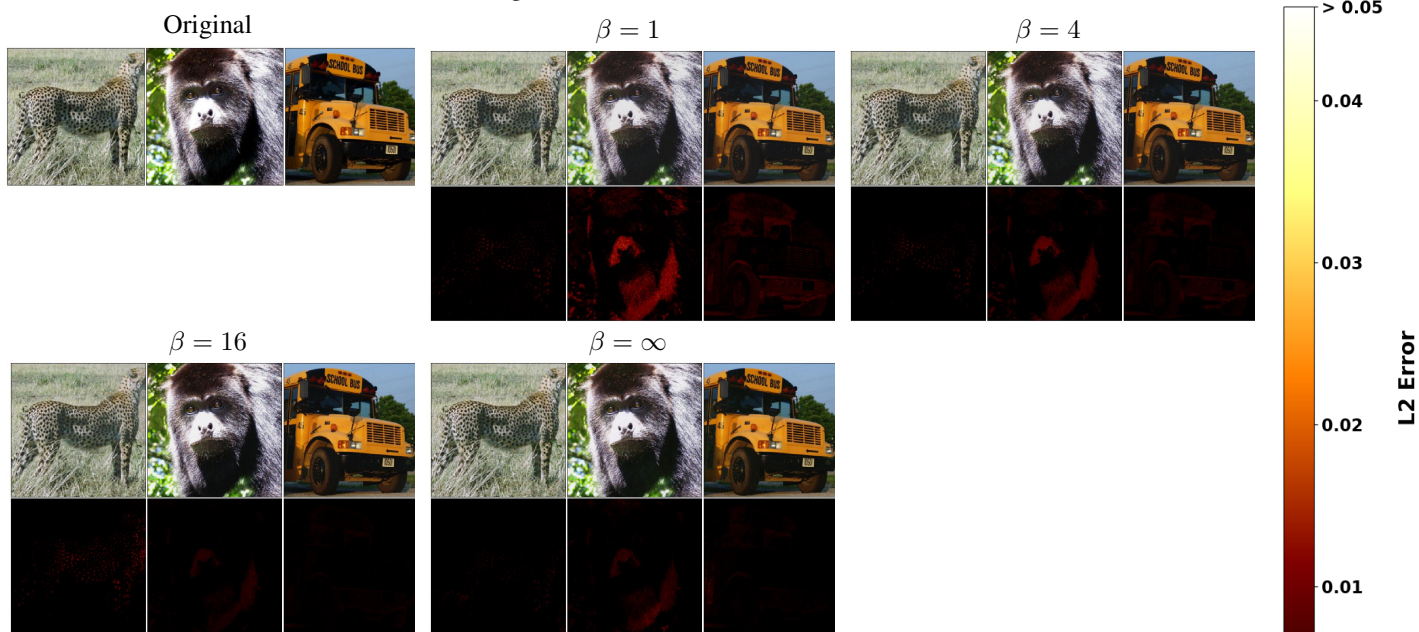


Figure 24: $\kappa = 0.01, d = 66$

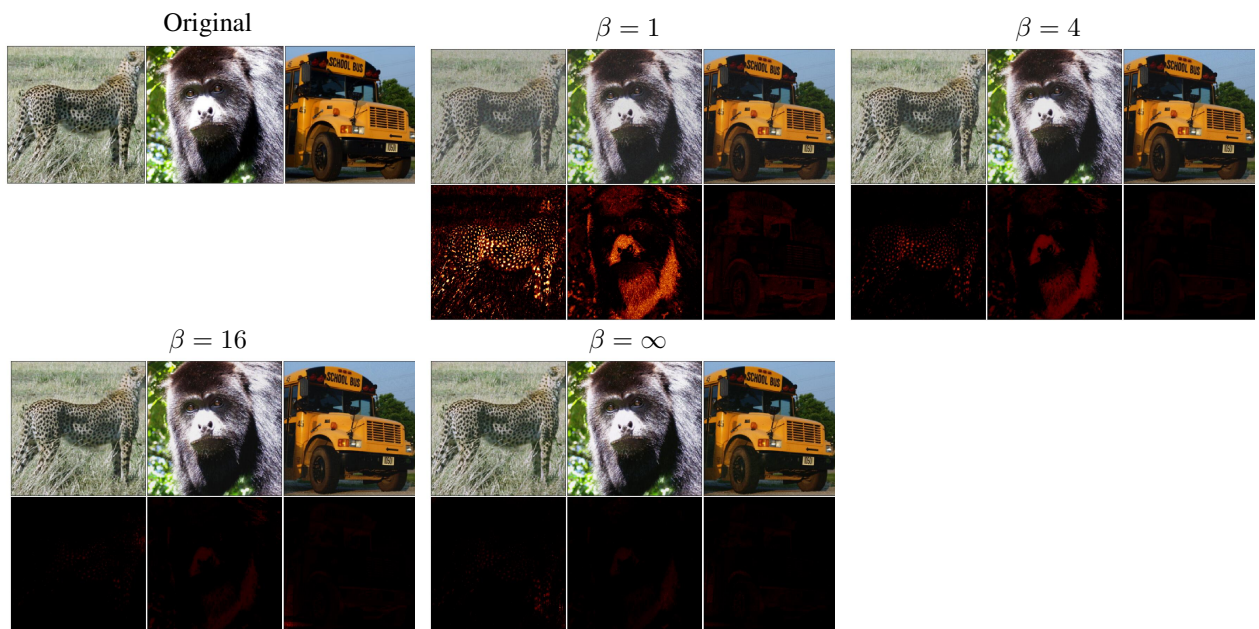


Figure 25: $\kappa = 0.01, d = 1000$

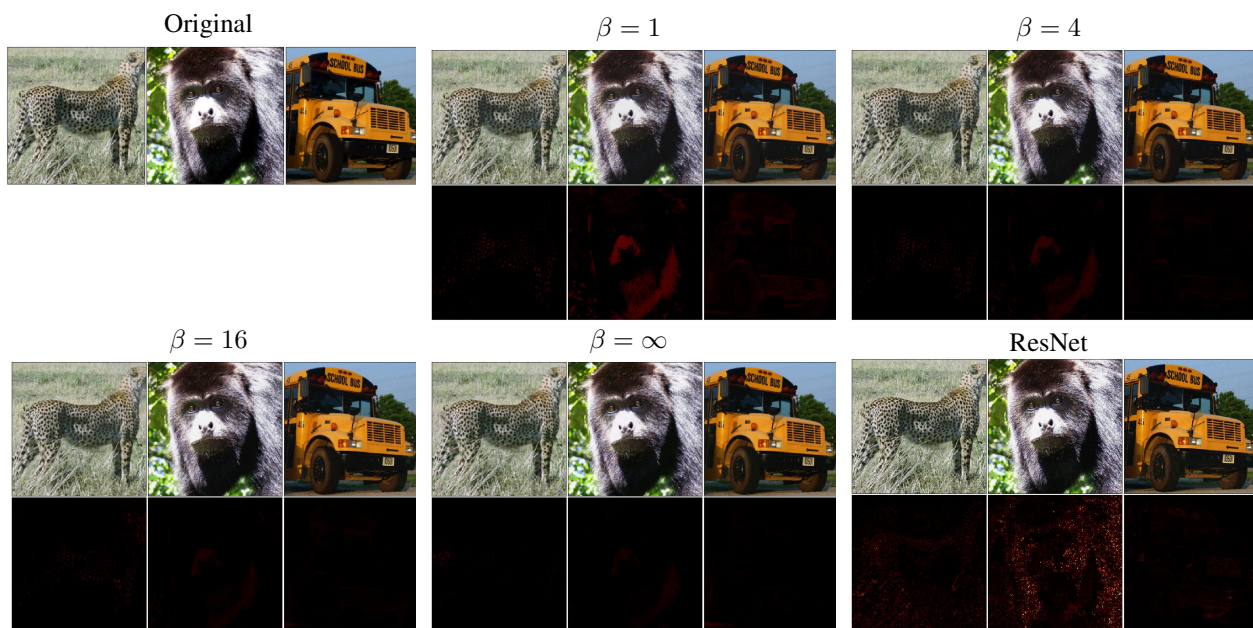


Figure 26: $\kappa = 1, d = 0$

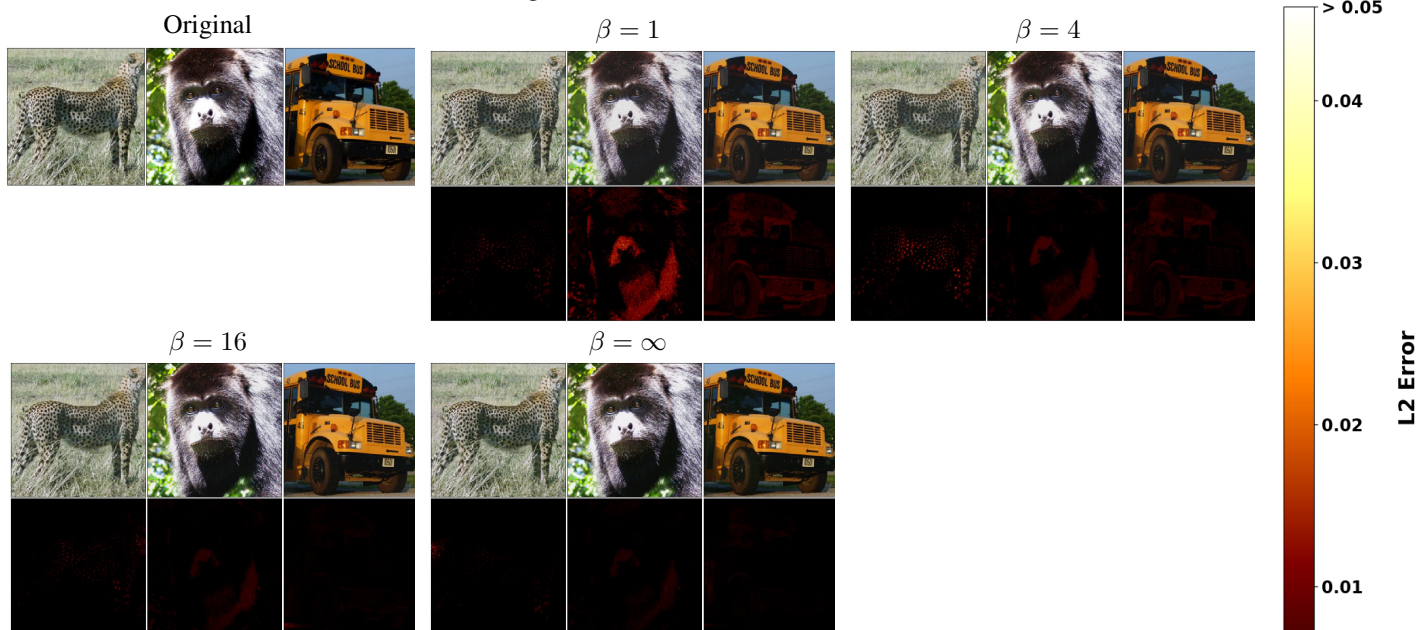


Figure 27: $\kappa = 1, d = 66$



Figure 28: $\kappa = 1, d = 1000$

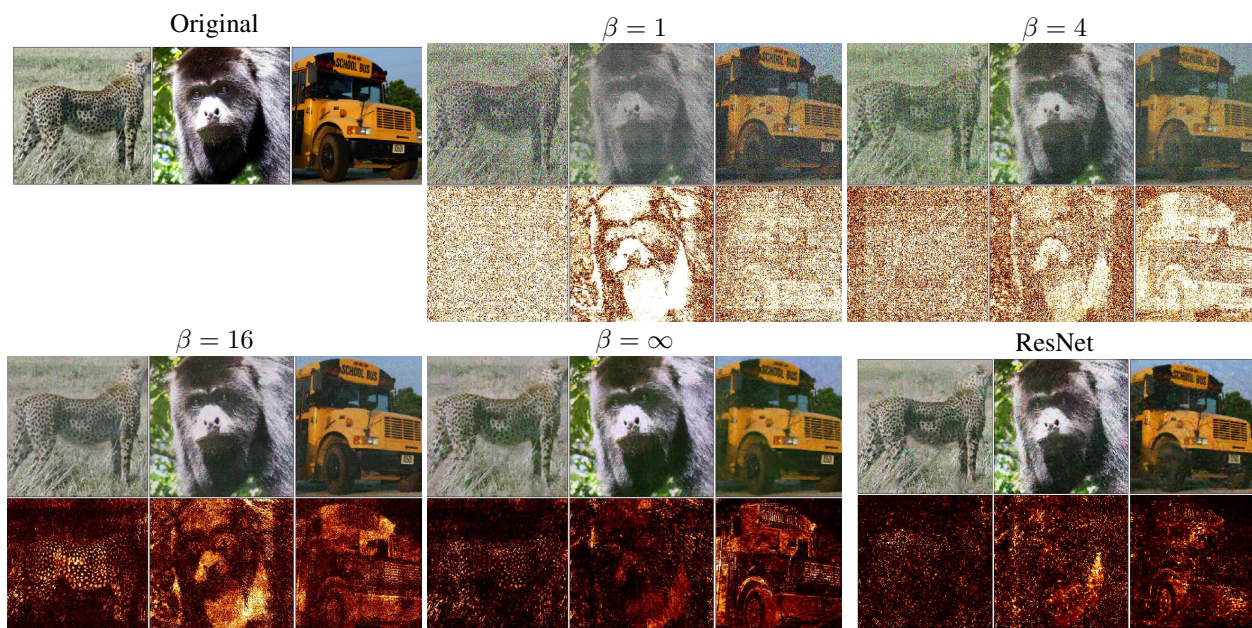


Figure 29: $\kappa = \infty, d = 0$

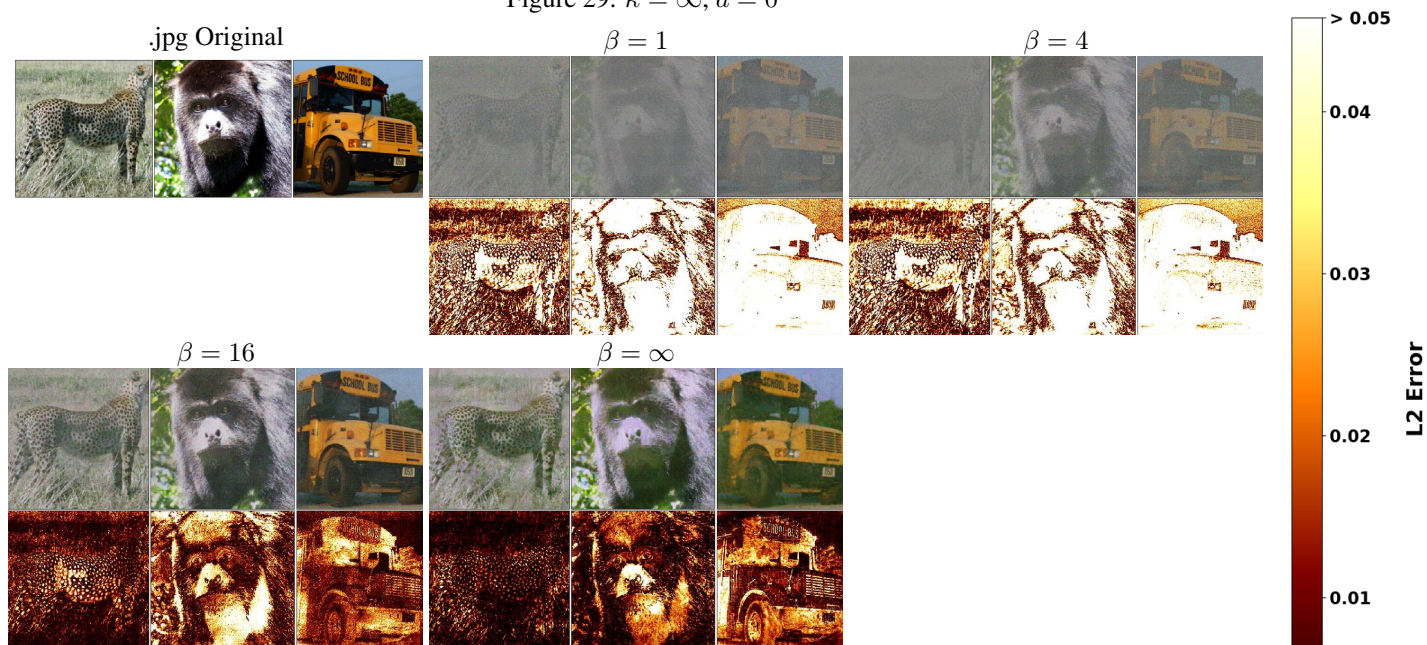


Figure 30: $\kappa = \infty, d = 66$

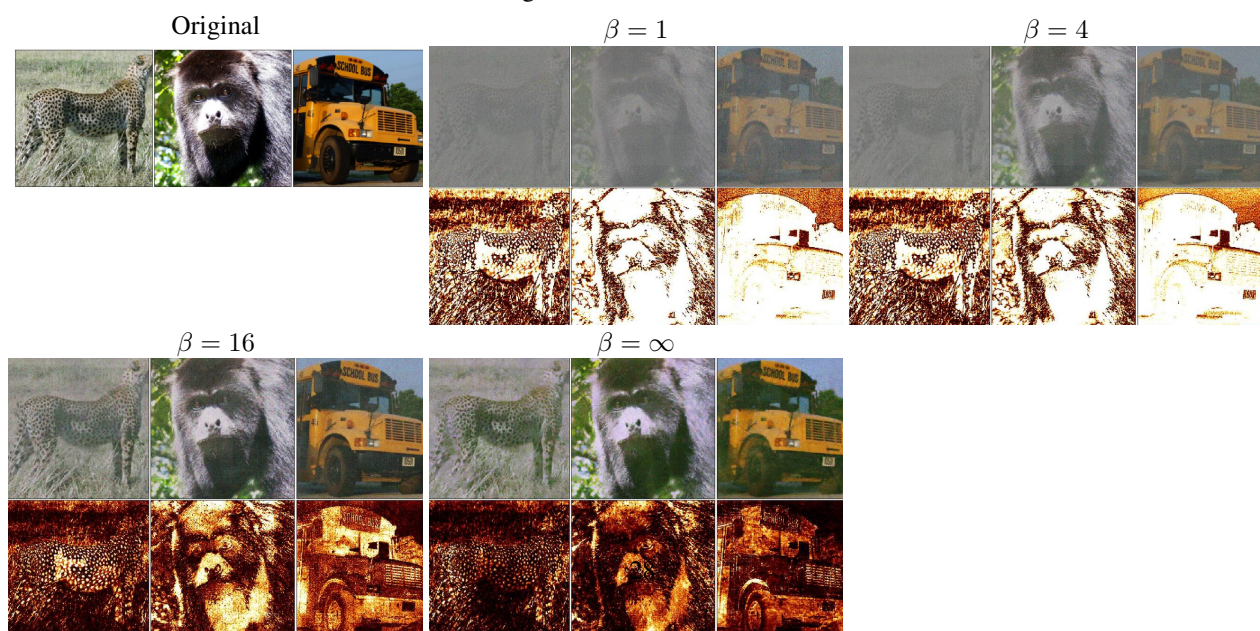


Figure 31: $\kappa = \infty, d = 1000$